Nuclear Instruments and Methods in Physics Research A 593 (2008) 376–398

Contents lists available at ScienceDirect

Nuclear Instruments and Methods in Physics Research A

journal homepage: www.elsevier.com/locate/nima

The alpha magnetic spectrometer silicon tracker: Performance results with protons and helium nuclei

J. Alcaraz [a], B. Alpat [b], G. Ambrosi [b], Ph. Azzarello [c,1], R. Battiston [b], B. Bertucci [b], J. Bolmont [i], M. Bourquin [c], W.J. Burger [b,*], M. Capell [d], F. Cardano [b], Y.H. Chang [e], V. Choutko [d], E. Cortina [c,2], N. Dinu [f], G. Esposito [b], E. Fiandrini [b], D. Haas [c], S. Haino [b], H. Hakobyan [c], M. Ionica [g], R. Ionica [h], A. Jacholkowska [i], A. Kounine [d], V. Koutsenko [d], G. Lamanna [b,3], A. Lebedev [d], C. Lechanoine-Leluc [c], C.H. Lin [e], M. Menichelli [b], S. Natale [c], A. Oliva [b], M. Paniccia [c], M. Pauluzzi [b], E. Perrin [c], M. Pohl [c], D. Rapin [c], M. Sapinski [i], I. Sevilla [a], W. Wallraff [j], P. Zuccon [b], C. Zurbach [i]

[a] Centro de Investigaciones Energéticas Medioambientales y Tecnológicas (CIEMAT), E-28040 Madrid, Spain
[b] INFN Sezione di Perugia and Università degli Studi di Perugia, I-06100 Perugia, Italy
[c] Université de Genève, CH-1211, Genève 4, Switzerland
[d] Massachusetts Institute of Technology, Cambridge, MA 02139, USA
[e] National Central University, Jhungli 320, Taiwan
[f] Institute for Space Science (ISS), R-76900 Bucharest, Romania
[g] Institute for Microtechnology (IMT), R-76900 Bucharest, Romania
[h] University Politechnica (UPB), R-76900 Bucharest, Romania
[i] Laboratoire de Physique Théorique et Astroparticules, IN2P3/CNRS, Université de Montpellier II, F-34095 Montpellier, France
[j] Physikalisches Insitut RWTH, D-52056 Aachen, Germany

ARTICLE INFO

Article history:
Received 23 October 2007
Received in revised form
1 May 2008
Accepted 6 May 2008
Available online 23 May 2008

Keywords:
Charged particle spectrometers
Tracking and position sensitive detectors
Cosmic-ray detectors
Spaceborne and space research instruments

ABSTRACT

The Alpha Magnetic Spectrometer is designed for a long duration measurement of the cosmic-ray spectra at an altitude of 400 km. The particle rigidity and specific energy loss are measured by a silicon tracker located in a 0.8 T field. Ground results for the position resolution, detection efficiency and charge determination for singly and doubly charged relativistic particles are presented and discussed in the context of the spaceborne detector.

0. Introduction

The Alpha Magnetic Spectrometer (AMS) is designed to operate at an altitude of 400 km on the International Space Station (ISS) [1]. The principal scientific objectives of the experiment are the searches for dark matter and antimatter with a precise measurement of the cosmic-ray composition in the energy range between 0.5 GeV and several TeV, for particle charges up to $Z = 26$. The instrument also operates as a gamma-ray observatory for photon energies above 1 GeV.

A first version of the device (AMS-01) was tested during a 10-day flight in June 1998 on the space shuttle *Discovery*. The experience acquired during the shuttle flight resulted in a considerable upgrade of the original design. The second generation detector (AMS-02), shown in Fig. 1, consists of a 0.8 T superconducting magnet, a silicon tracker, a transition radiation detector (TRD), a time-of-flight (TOF) system composed of plastic scintillators, a ring-imaging Cherenkov detector (RICH) and an electromagnetic calorimeter (ECAL). The central tracking region is surrounded by anti-coincidence counters (ACC).

The modular design of the silicon tracker results in a performance characterized by the behavior of its basic functional elements, the silicon ladders. The position resolution is defined effectively by the strip implantation scheme of the silicon sensors.

* Corresponding author.
E-mail address: william.burger@cern.ch (W.J. Burger).
[1] Now at INFN-Perugia, Italy.
[2] Now at CIEMAT, Madrid, Spain.
[3] Now at Le Laboratoire d'Annecy-le-vieux de Physique des Particules, F-74941 Annecy-le-Vieux Cedex, France.

0168-9002/$ - see front matter © 2008 Elsevier B.V. All rights reserved.
doi:10.1016/j.nima.2008.05.015

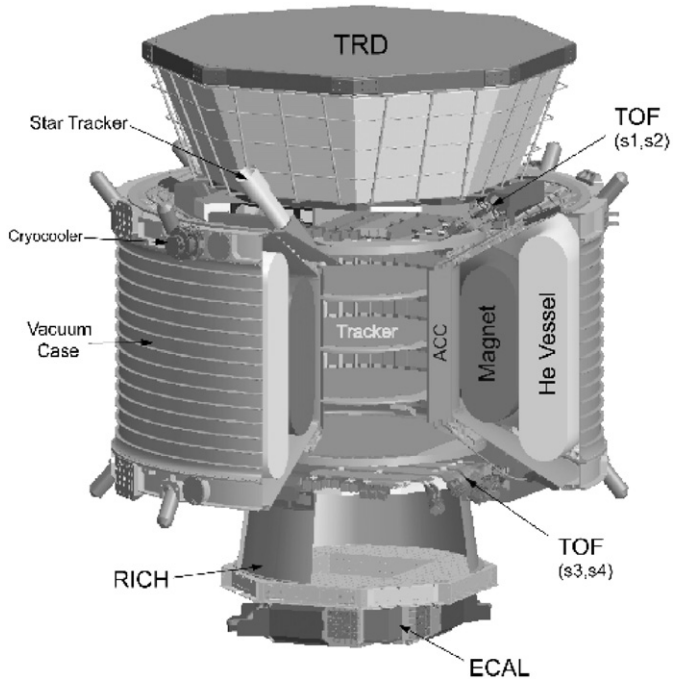

Fig. 1. AMS-02.

The final performance depends critically on the noise level of the readout strips at the input of the frontend electronics. A second important parameter affecting the signal-to-noise ratio is the hold delay used to sample the output of the frontend preamplifier.

After a description of the silicon tracker (Section 1) and the particle beam measurements with the AMS-02 silicon ladders (Section 2), the calibration procedure and data processing are described, and the noise performance is presented (Section 3). The specific energy loss of singly charged, minimum ionizing particles is the minimum bias signal. Therefore, the hold delay is defined with respect to the performance for relativistic protons (Section 4). The position measurement is based on the relative amplitudes of the signals of the readout strips and reflects the details of the charge-sharing in the silicon (Section 5). An optimal performance implies good position resolution with high detection efficiency (Section 6).

The silicon tracker provides multiple measurements of the specific energy loss which are combined with the velocity measurements of the TOF scintillators and the RICH to define the particle charge. The performance results reported for relativistic helium nuclei (Section 8) were obtained in secondary ion beams, where the particle charge was identified unambiguously using the specific energy losses recorded in the silicon ladders (Section 7).

The paper concludes with a discussion on the consequences of the particle beam results for the performance of the superconducting magnet spectrometer on the ISS, with respect to the constraints imposed on the spaceborne detector (Section 9).

1. The silicon tracker

The tracker is composed of silicon microstrip sensors, which were developed to provide precise tracking (o 10 mm resolution) in experiments performed at particle accelerators. Among the advances in the field, the following are important in the present application: the use of capacitive charge coupling to improve the charge collection across the readout gap, thus providing the desired resolution with a practical readout density [2]; the introduction of p^+ blocking strips on the ohmic side to provide two-dimensional information from a single wafer thickness [3]; the development of thin-film cables which limit the material thickness in the active region of the detector [4]; and low-noise frontend electronics, which is capable to handle the high inter-strip capacitance associated with the long effective strip lengths of large area detectors [5].

Table 1
Characteristics of the AMS-02 silicon sensors: strip leakage current (I_{ss}), guard ring to strip resistance (R_{gs}), inter-strip resistance (R_{is}) and inter-strip capacitance (C_{is})

	p-side	n-side
I_{ss}	300 pA	3 nA
R_{gs}	≈ 50 GO	≈ 1 GO
R_{is}	≈ 500 GO	≈ 10 GO
C_{is}	2 pF/cm	1 pF/cm

1.1. Silicon sensors

The AMS-02 tracker contains 2264, 41:360 × 72:045 × 0:300 mm^3, double-sided microstrip sensors[4] obtained from n-type, high resistivity (4 6 kO cm) circular silicon wafers with ⟨1 1 1⟩ lattice orientation. The sensors are biased via the punch-through technique [3]. The 14 mm wide p-side (junction) strips have implantation and readout pitches of 27.5 and 110 mm; the 15 mm wide n-side (ohmic) strips have implantation and readout pitches of 52 and 208 mm. The average values of the important noise performance parameters, based on the measurements of ~1500 AMS-02 sensors [6], are reported in Table 1.

The AMS sensor dimensions and design are similar to the sensors of the vertex detectors at the Large Electron-Positron (LEP) collider at CERN [7], and in analogy to the LEP detectors, the silicon sensors are grouped together to form independent mechanical and functional units (ladders) with a common readout and bias voltage [8]. The number of sensors in an AMS ladder varies between 7 and 15. The different ladder lengths are required to match the cylindrical shape of the magnet, a geometry which maximizes the acceptance-to-weight ratio. The maximum readout strip length attains 60 cm, which may be compared to the 72 cm long silicon ladders of the NOMAD-STAR detector [9], at present the reference in the field.

1.2. Frontend electronics

The readout strips of the AMS silicon sensors are ac-coupled to the low noise, high dynamic range frontend readout chip, the VA version *Hdr9A*[5] of the original Viking design [5], by 700 pF capacitor chips. Each VA readout channel consists of a charge-sensitive amplifier, a CR-RC semi-Gaussian shaper and a sample-and-hold stage. The equivalent noise charge for a given capacitive load (C) was measured to be (350 + 4C=pF) electrons with a 6 ms delay hold time, i.e. the difference in time between the passage of the particle in the silicon and the sampling of the signal at the output of the shaper. In practice, once the operating currents have been established in order to satisfy the power consumption criteria (~0:5 mW=channel), a final optimization of the hold delay is made.

[4] Colibrys SA, Maladière 83, 2000 Neuchâtel, Switzerland.
[5] Gamma Medica-Ideas AS, Martin Linges vei 25, Snaroy, POB 1, N-1330 Fornebu, Norway.

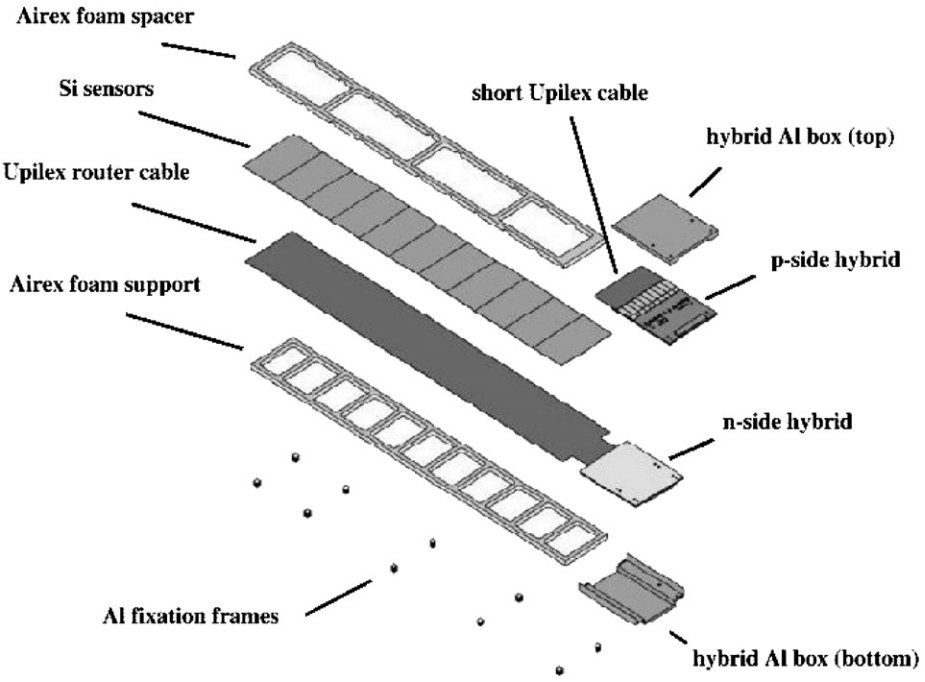

Fig. 2. The principal components of the silicon ladder.

1.3. The ladder design

The VA and capacitor chips are located on a standard printed circuit board (hybrid) which is connected to the ladder by a 50 mm thick flexible upilex cable[6]; the p-side (n-side) hybrid contains 10 (6) 64-channel VA chips. The n-side cable extends over the length of the ladder and redirects the signals of the n-side strips (oriented orthogonally to the ladder length) to the hybrid.

The routing scheme of the n-side cable distributes the strip signals of alternating sensors to the same readout channel, i.e. the 192 channels of the first (second) three VAs receive the signals from the readout strips of sensors 1, 3, 5 y (2, 4, 6 y). The resulting ambiguity is resolved by a change of the readout pitch (104 mm) in selected regions of the external plane ladders, which introduces a shift of the readout strip scheme with respect to the ladders on the internal planes.

A foam support[7] is glued to the longer n-side upilex cable. Small 5 mm^3 aluminum frames are glued to the 100 mm thick carbon fiber skin which covers the exposed side of the foam support. The aluminum frames contain a threaded screw hole which is used to fix the ladders to the tracker planes. A second foam spacer is added to the p-side. An electromagnetic shield, a 50 mm thick metalized upilex foil, surrounds the silicon sensors. The hybrids are enclosed in a 0.3 mm thick aluminum box.

The principal components of the ladder are indicated in Fig. 2. Fig. 3 shows a view of the n-side of a seven-sensor-long ladder.

1.4. The tracker structure

The AMS-02 tracker contains 192 ladders arranged in eight layers on five circular support planes composed of a low density aluminum honeycomb structure enclosed within thin carbon fiber skins (Fig. 4). The first and last support planes are located outside the magnet and have a diameter of 1.4 m and an average density of 0:032 g=cm^3. Planes 2–4, located inside the magnet, have a diameter of 1 m and an average density of 0:016 g=cm^3. Ladders are mounted on both sides of the inner support planes. The first and last silicon layers are separated by a distance of 1.06 m.

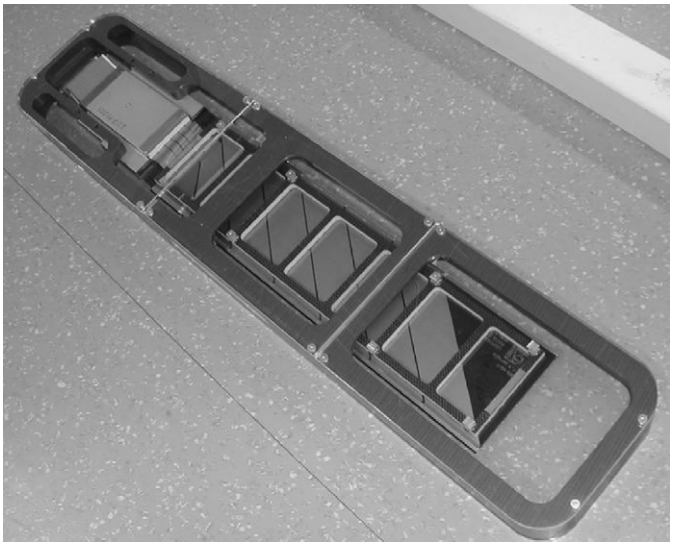

Fig. 3. View of the n-side of a seven-sensor-long AMS-02 ladder in its storage/transportation box.

Fig. 5 shows a detailed view of the shielded ladders on an internal tracker plane. The flexible upilex cables, which connect the readout strips of the silicon sensors to the frontend electronics, allow to incline the hybrids by 90°, thus limiting the material thickness in the detector acceptance.

A summary comparison of the AMS-02 tracker, with a representative sample of silicon strip trackers of accelerator-based experiments and spaceborne detectors, is presented in Table 2.

[6] UBE Europe GmbH, Immermannstraß 65B, 40210 Düsseldorf, Germany.
[7] Airex AG Specialty Foams, CH-5643 Sins, Switzerland.

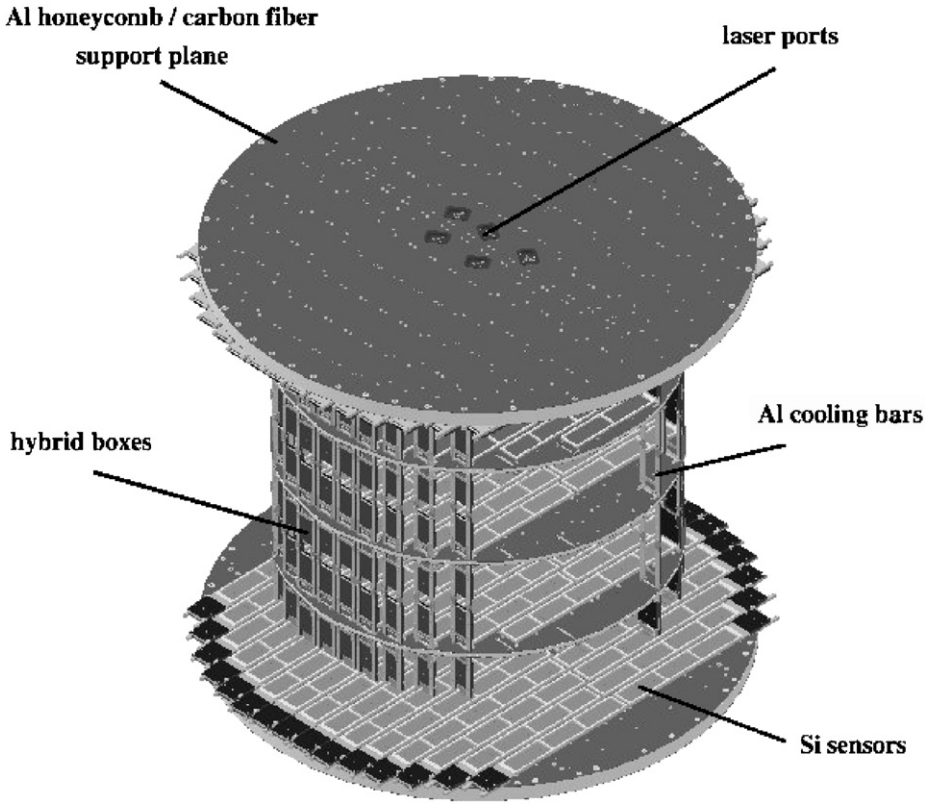

Fig. 4. The AMS-02 silicon tracker; the carbon fiber support structures, a cylindrical shell enclosing the internal planes and two conical flanges which support the external planes, are not shown.

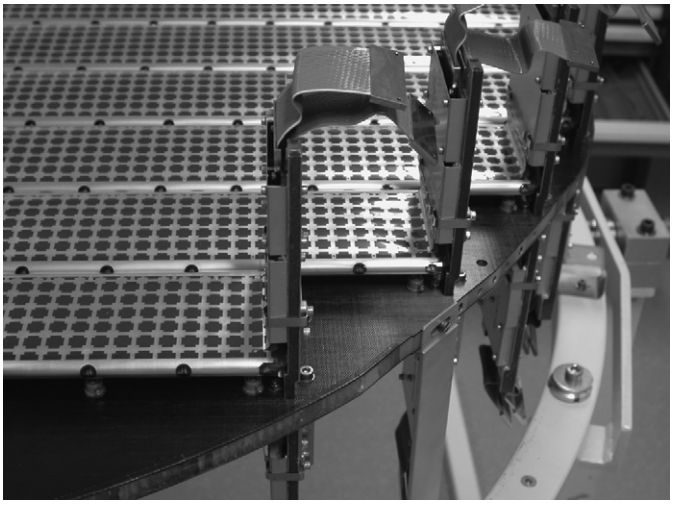

Fig. 5. Detailed view of the shielded silicon ladders in their final configuration on an inner tracker plane.

2. Particle beam data

In June 2003, four AMS-02 ladders were operated in a proton beam at the CERN Proton Synchrotron (PS) to study the influence of the VA hold delay on the performance for singly charged, minimum ionizing particles. A six ladder telescope was placed in proton and ion beams at the CERN Super Proton Synchrotron (SPS) in October 2002 and 2003. In September 2004, a four ladder telescope and an 11 ladder tracker were used to study the photon detection capabilities via pair production in an electron beam at the CERN PS. The relevant parameters of the particle beam measurements are listed in Table 3.

Table 2
Active area and readout strip pitch of the silicon strip trackers of different high energy physics experiments and spaceborne particle detectors

	Active area (m^2)	Readout pitch (mm)
LEP experiments	0.5–1.4	50
NOMAD-STAR	1.14	50
D0/CDF	3/6	50/60
ATLAS	60	80 (binary)
CMS	200	100
PAMELA	0.13	50
AMS-02	6.75	110
AGILE	4	242
GLAST	73.8	228 (binary)

The ATLAS and GLAST trackers use a binary readout (the addresses of the strips over threshold).

Table 3
Particle beam parameters: particle type and rigidity, VA hold delays, the number of ladders present and their orientation with respect to the beam direction, 0° angle corresponding to normal incidence

Date	Particle	Rigidity (GV)	Hold delay (ns)		Ladders	Angles (1)
			p-side	n-side		
October 2002	p	7–15	4.5	4.5	6	0, 15, 30
	He	40	4.5	4.5	6	0, 15, 30
June 2003	p	10	1–8	1–8	4	0
October 2003	p	7–15	3	4	6	0
	He	40	3	4	6	0
September 2004	e^-	3–7	3.5	4.5	16	0

For the 2002 and 2003 measurements, the data acquisition hardware consisted of a custom-designed interface card to manage the trigger and readout, and preliminary versions of the Tracker Data Reduction (TDR) card. The TDR contains 12-bit

analog-to-digital converters (ADC), data buffers and digital signal processors (DSP), which are programmed to perform calibration and data reduction. The TDRs were operated in raw mode, i.e. no online data reduction was performed and the digitized output of all channels was recorded. Out-of-spill data were used to perform an offline calibration to determine the individual channel pedestal and noise values.

The silicon ladders were mounted in a light-tight aluminum box containing thin aluminum foil windows. The hybrids were connected to the TDRs by 1 m long flight quality cables. The TDRs were located in a prototype crate. The VA operating voltages, the TDR power and the silicon sensor bias voltage (80 V) were supplied by preliminary versions of the tracker power supplies. The data acquisition computer, as well as the TDR crate and the power supplies, were located in the experimental area. A second computer was used to control and monitor the detectors remotely.

Flight versions of the TDRs and tracker power supplies were used in September 2004. In addition to a four ladder telescope, a second light-tight aluminum box placed in a 0.4 T dipole magnet contained an 11 ladder tracker in the AMS-02 configuration, i.e. eight layers of silicon ladders mounted on five aluminum-honeycomb-carbon-fiber supports with the appropriate inter-plane spacing. An additional ladder was placed downstream of the magnet in front of a module of the AMS-02 ECAL.

The upstream telescope provided the direction of the electrons incident on a tungsten foil located at the entrance of the magnet. The trajectories of the beam electrons and the $e^{\pm}$ conversion pairs of the bremsstrahlung photons produced in the tungsten were reconstructed in the tracker. The 16 ladders were read out with a single TDR crate. Data reduction and calibration were performed by the DSPs.

3. Data processing

The ADC values of the readout strips include the following contributions: a constant offset (pedestal), a coherent (common) noise component, the strip noise and an eventual signal, i.e. the charge accumulated on the strip due to the passage of an ionizing particle in the depleted silicon. The strip pedestal and noise values are determined during the calibration. The common noise is computed at the level of the VAs for each event. A valid signal is defined by the threshold applied to the strip signal-to-noise ratio, where signal refers to the ADC value after pedestal and common noise subtraction.

3.1. Calibration procedure

The calibration procedure consists of a series of summations over the raw and subsequently modified ADC values for a predefined number of random trigger events. The first series establishes the preliminary values of the strip pedestals and standard deviations (s). The final strip pedestals are computed during the second series by restricting the summation to ADC values within ± 3s of the preliminary values. In a third series, the strip pedestals are subtracted and the standard deviations (s_{raw}) of the noise (common and strip) are computed with ADC values limited to ± 3s around the pedestals. Strips with abnormally large or low standard deviations are flagged and excluded from the common noise determination. A fourth series of events is used to compute the strip noise (s_{ped}) after subtraction of the pedestals and common noise, and the requirement that the modified ADC values do not exceed $\pm 3s_{raw}$. In a final series, non-Gaussian channels are identified by applying a ns_{ped} threshold to a statistically significant number of events. In addition, the results of the common noise determination are tabulated yielding the average value and standard deviation for each VA.

The common noise may be influenced by the presence of bad strips and/or an ionizing particle in non-random trigger events. The former are identified during the calibration and excluded. The effect of the latter is negligible. The signal levels of relativistic singly charged particles ($\sim$30 ADC counts) distributed over the 64 channels of the VA represent a small offset; for higher particle charges, the eventual bias represents a proportionally small, negligible fraction of the signal. Therefore, no attempt is made to take into account the presence of an eventual signal in the common noise calculation.

3.2. Calibration results

The average strip noise for the four ladders in the June 2003 test beam were 2.76 and 3.56 ADC counts on the p- and n-sides. The calibration data, which were accumulated at regular intervals during 2.5 days with a random trigger outside the beam spill, display a correlation between the strip noise and the daily temperature variations in the experimental hall (Fig. 6). A linear correlation is observed between the strip noise and temperature between 25 and 32 °C, with coefficients of 0.015–0.020 and 0.030–0.045 ADC counts/1C for the p- and n-sides, respectively (Fig. 7).

The average strip noise for the six ladders present in the October 2003 test beam were 2.53 and 3.09 ADC counts on the p- and n-sides. The proton beam data were taken with stable operating conditions ($20{:}5 \pm 0{:}1$ °C) and no significant variation was observed in the noise levels.

Readout strips with a noise level exceeding five ADC counts are flagged as "high noise" strips. The average fractions of high noise strips of the 10 ladders, i.e. strips flagged as high noise in at least 50% of the calibrations, were 0.7% and 3.3% on the p- and n-sides. The average fraction of dead channels was, respectively, 0.5% and 2.4%.

The influence of high noise channels on the performance is limited essentially to the measurement of the singly charged particle spectra. With respect to the cosmic-ray nuclei performance, the average pedestal values and their standard deviations define the effective dynamic range in the 12-bit ADC. Consequently, an effort has been made to optimize the VA performance for these parameters. The average values for the p- and n-sides for the 10 AMS-02 ladders are 418 ± 69 and 408 ± 74 ADC counts; the corresponding values of the AMS-01 ladders were 1145 ± 237 and 896 ± 249.

4. VA hold delay and performance

The influence of the VA hold delay on the performance was studied with four ladders in a 10 GV proton beam at the CERN PS in June 2003. Simple selection criteria are used to obtain unbiased results over the interval 1–8 ms. The track reconstruction requires a single pn cluster pair in each ladder. A cluster is defined with at least one seed strip with a signal-to-noise level above or equal to $4s_{ped}$. If multiple, the seed strips must be contiguous. Neighboring strips are added to the cluster if their signal-to-noise level exceeds s_{ped}. In the case of single strip clusters, the neighboring strip with the highest positive (after common noise and pedestal subtraction) signal is added.

The specific energy loss (cluster charge) distributions, associated with reconstructed tracks, of the downstream ladder (position 4) are shown in Fig. 8 for 11 values of the hold delay between 2 and 8 ms. The most probable specific energy loss is obtained by fitting the distributions with a Landau function

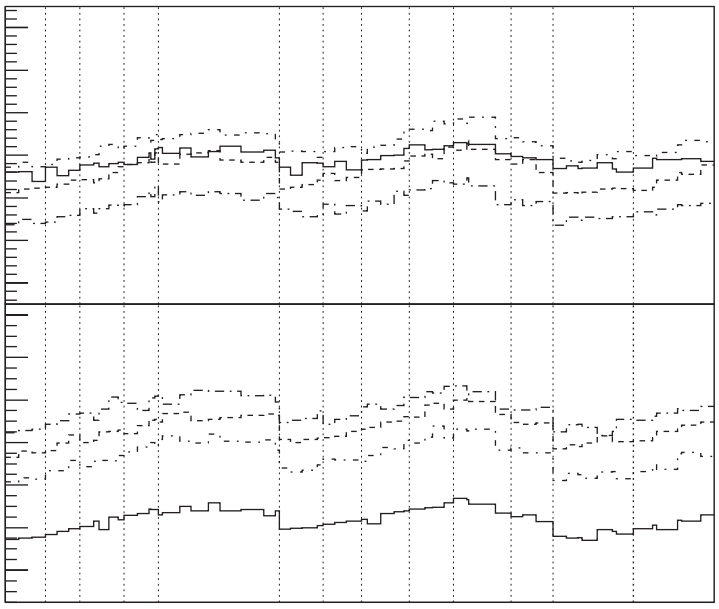

Fig. 6. The evolution in time (hour and minutes indicated) of the average strip noise of the four ladders present in the June 2003 test beam. The noise levels display a daily variation due to the temperature changes in the experimental hall. The corresponding VA hold delays of the different data periods are indicated at the top.

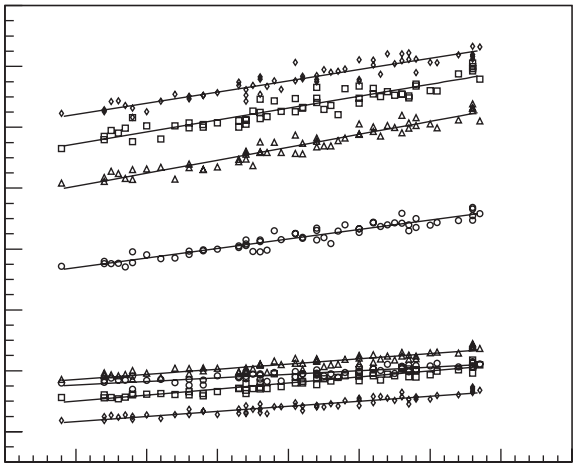

Fig. 7. The temperature dependence of the average strip noise of the four ladders present in the June 2003 test beam.

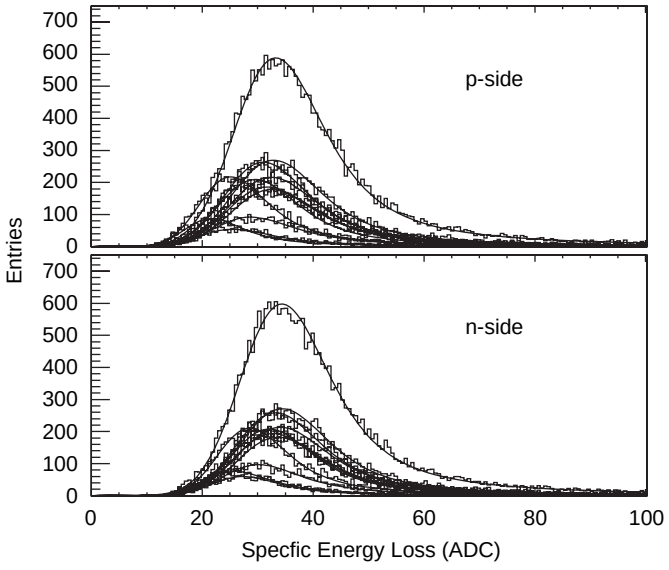

Fig. 8. The specific energy loss distributions for different VA hold delays of the ladder occupying position 4 in the June 2003 test beam. The value of the most probable energy loss is obtained by fitting the data with a Landau function convoluted with a Gaussian noise contribution.

convoluted with a Gaussian noise contribution [11]. The most probable values are shown in Fig. 9. The optimal signal levels are observed at 4 and 4:5 ms on the p- and n-sides, respectively. The ladders display a satisfactory uniformity in response.

The average number of clusters per event (cluster multiplicity) and the average cluster size (strip multiplicity) as a function of the hold delay are shown in Fig. 10. The selection efficiencies tend to decrease above 5 ms. The observed low efficiencies and abnormally large clusters indicate a lower operational limit of ~2 ms.

The average cluster characteristics of the four ladders, corresponding to delay holds of 4 and 4:5 ms for the p- and n-sides, are listed in Table 4. The cluster signal-to-noise is defined as the total cluster charge divided by the root-mean-square of the noise of the member strips: $[\sum_i s_{(i)}]/[\sum_i s^2_{\mathrm{ped}(i)}]^{1/2}$, where $s_{(i)}$ and $s_{\mathrm{ped}(i)}$ are the strip signal and noise.

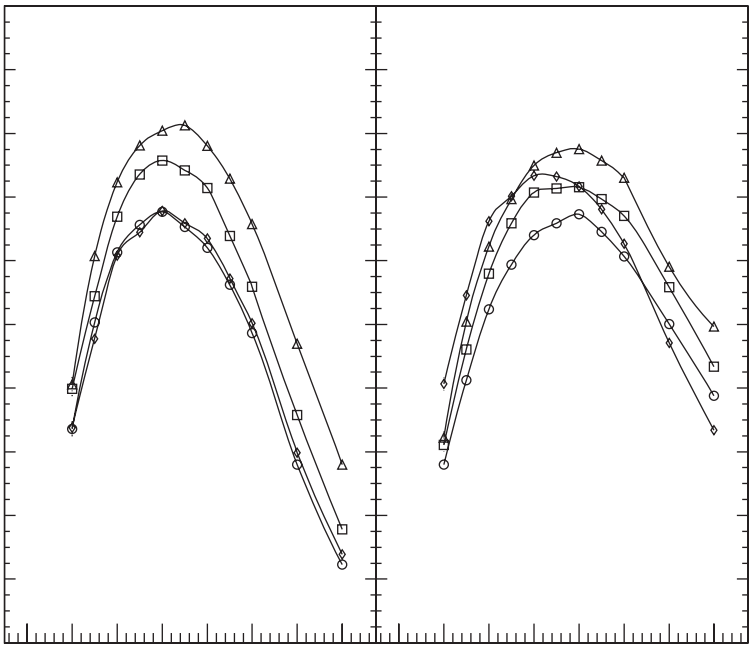

Fig. 9. Most probable specific energy loss as a function of the VA hold delay for the four ladders present in the June 2003 test beam.

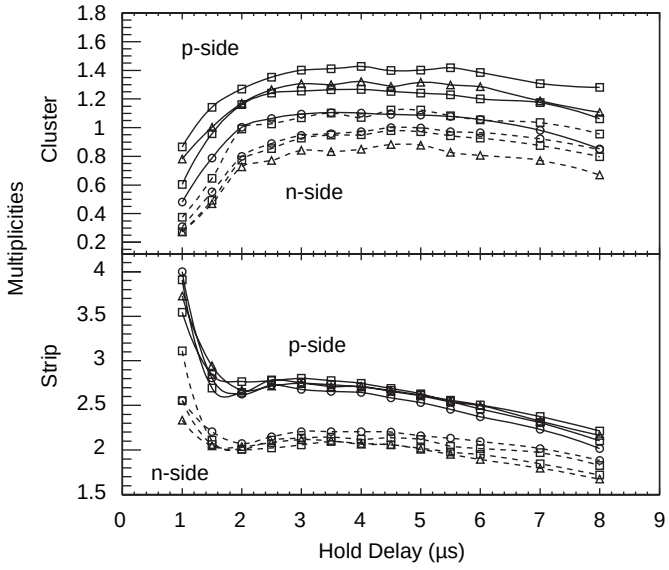

Fig. 10. The variation of the cluster multiplicity per event (top) and cluster strip multiplicity (bottom) with the VA hold delay for the four ladders present in the June 2003 test beam.

5. Position resolution

The coordinates of the selected np cluster pairs are given by the position of the sensor along the beam direction (z) and the vertical (y) and horizontal (x) positions determined, respectively, on the p- and n-sides of the silicon by the signal-weighted mean of the positions of the two highest signal-to-noise strips of the cluster. The orientation of the coordinate axis is defined by the strips of the most upstream ladder (position 1). In the June 2003 data, a correction is applied to account for the relative orientation in the

Table 4
Characteristics of the selected proton clusters: most probable signal, most probable signal-to-noise, average cluster size (number of strips) and average cluster multiplicity per event

Side	Delay hold (ms)	Signal (ADC)	s/n	Size	Mult
June 2003					
p	4.0	32.6	7.4	2.7	1.28
n	4.5	32.4	6.3	2.1	1.00
October 2003					
p	3.0	26.5	6.7	2.7	1.03
n	4.0	32.6	7.0	2.4	0.96

xy plane of the strips of the ladders in positions 1 and 4. The ladders in positions 2 and 3 are aligned (displacements along x and y and rotations about the principal axes) with respect to the positions of ladders 1 and 4. The nominal values are used for the relative distances between the ladders along the beam direction (5 cm).

Figs. 11 and 12 show the x and y residual distributions at the four ladder positions for the data taken with a 4 ms hold delay. The residual is defined as the difference between the measured track position and the position obtained by a line fit in the xz and yz projections. Background and noise clusters are identified by comparing the consistency of the beam divergences obtained with all two-point combinations. The consistency check eliminates a relatively small flat background (o 0:1%).

The residual distributions are described by a sum of two Gaussians which are centered near zero: $-0{:}1 \pm 0{:}4$ (narrow) and $0{:}2 \pm 0{:}9$ mm (broad) on the p-side, $0{:}1 \pm 0{:}7$ (narrow) and $-0{:}2 \pm 1{:}3$ mm (broad) on the n-side. The relative area of the narrow Gaussian represents 73% and 77% of the total area of the two Gaussians on the p- and n-sides, respectively.

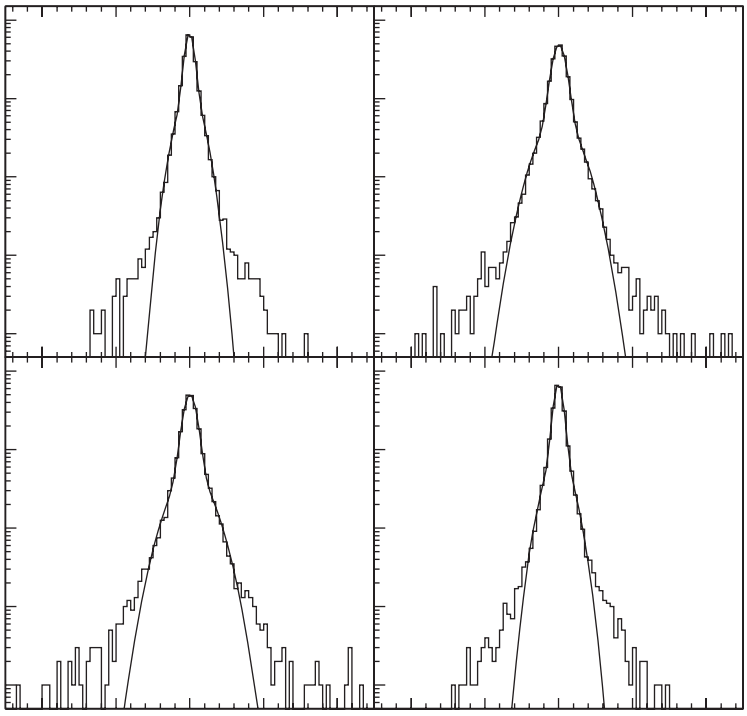

Fig. 11. The p-side residual distributions (four point fit) at the four ladder positions for the 4 ms hold delay data of the June 2003 test beam. The residual distributions are described with a sum of two Gaussians; the narrower Gaussian width (s_1) and the area-weighted average width of the two Gaussians are indicated (s_{12}).

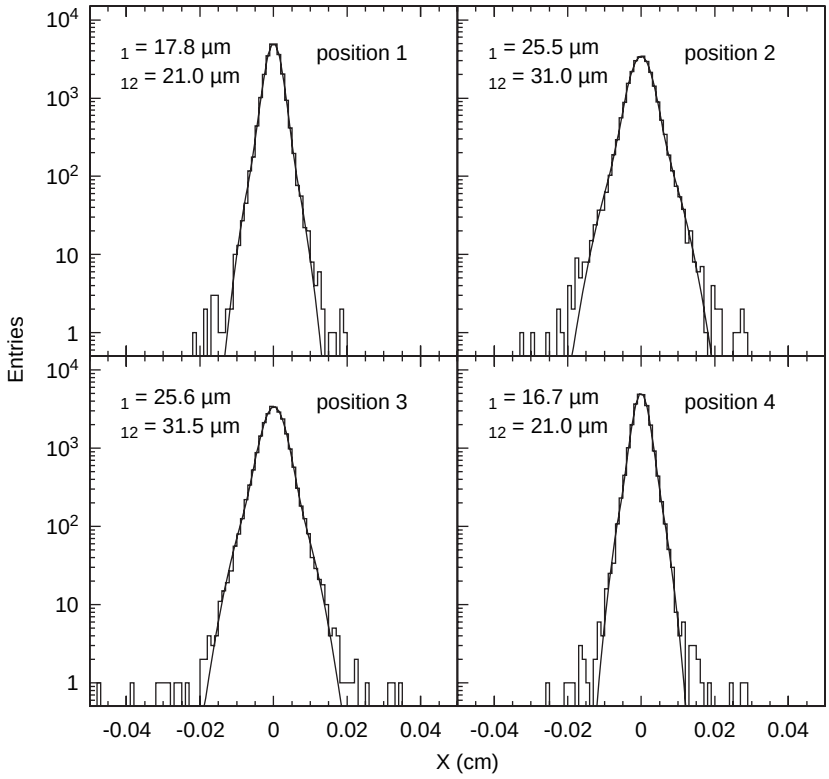

Fig. 12. The n-side residual distributions (four point fit) at the four ladder positions for the 4 ms hold delay data of the June 2003 test beam. The residual distributions are described with a sum of two Gaussians; the narrower Gaussian width (s_1) and the area-weighted average width of the two Gaussians are indicated (s_{12}).

5.1. Resolutions from residuals

The width of the residual distribution is a good estimate of the detector resolution when better resolution detectors are used to provide the projected track position. In the present case, the uncertainty of the projected track position represents a non-negligible contribution. With the assumption that the resolutions of the ladders are the same, an average ladder resolution is obtained by comparing the observed residual distributions at the four ladder positions with those of a Geant3 [12] simulation, where nominal resolutions, the widths of Gaussian distributions, are used to randomize the track coordinates.

In the simulation, the resolutions of the four ladders are varied simultaneously between 2.5 and 25 mm for the p-side and between 15 and 60 mm for the n-side. The generated residual distributions are described by a single Gaussian. The correlation between the residual widths and position resolution is linear over each range, however, separate fits are used to characterize the relation residual-resolution on the two sides of the silicon (Fig. 13).

The residual distributions for three and four point fits are compared to check the consistency of the results, consequently two groups of lines are present in Fig. 13. Slopes larger than unity correspond to the results obtained without the ladder in the fit, while slopes smaller than unity correspond to the results obtained with the four point fit.

The narrow Gaussian widths (s_1) of the two-Gaussian fits of the residual distributions determine the position of the data point along the lines in Fig. 13. The distributions of the ladder resolutions, i.e. the corresponding abscissa values, appear below the two-dimensional plot. The average resolutions are $9{:}8 \pm 0{:}3$ and $30{:}7 \pm 1{:}0$ mm for the p- and n-sides. The quoted uncertainties correspond to the standard deviation of the mean values obtained by combining the results of the four ladders for the two fits. The resolutions corresponding to the area-weighted average residual widths are $15{:}3 \pm 0{:}6$ and $37{:}7 \pm 0{:}5$ mm, respectively.

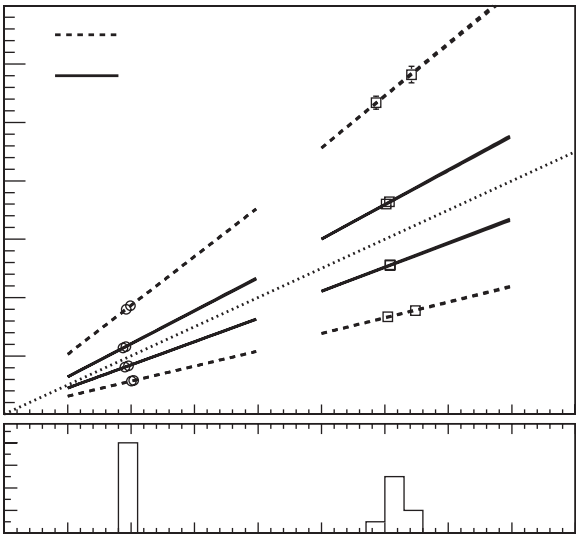

Fig. 13. The relation between residual widths and position resolution at the four ladder positions in the June 2003 test beam. The lines with slopes larger (smaller) than unity correspond to the three (four) point track fits. The individual ladder resolutions, corresponding to the experimental narrow Gaussian residual widths, are given by the abscissa values of the data points for the p- (○) and n-sides (&). The distributions of the latter, the average values and standard deviations are shown at the bottom.

Fig. 14 shows the effect of the VA hold delay on the resolution, i.e. the narrow Gaussian widths of the residual distributions. The optimal p-side performance is observed between 4 and 5 ms. The n-side resolution is rather insensitive to the hold delay; the optimal range extends from 4 to 6 ms.

The proton residual distributions for the six ladder telescope used in the October 2003 test beam, and the two-Gaussian fits, are shown in Figs. 15 and 16. The cluster selection and track reconstruction criteria are identical to those used for the June 2003 data. The alignment was performed in the same manner with the ladders in positions 1 and 6 occupying the roles of the ladders in positions 1 and 4 in the four ladder configuration. The average positions of the two Gaussians are $0{:}2 \pm 0{:}5$ (narrow) and $-0{:}4 \pm 0{:}6$ mm (broad) on the p-side, $0{:}1 \pm 1{:}2$ (narrow) and $-0{:}2 \pm 2{:}8$ mm (broad) on the n-side. The relative area of the narrow Gaussian represents 71% and 90% of the total area of the two Gaussians on the p- and n-sides, respectively. The October data were taken with VA hold delays of 3 and 4 ms on the p- and n-sides (Table 3).

The resolutions corresponding to the narrow Gaussian residual widths are presented in Fig. 17. The correlations between residual width and resolution are different for the ladder pairs occupying the positions 1–6, 2–5 and 3–4 due a non-symmetry in the six-ladder configuration. The mechanical support structure provided five equally spaced positions along the beam direction. The ladder located at one of the outermost positions is separated by 8.5 cm from the adjacent ladder; the larger clearance allows to rotate the ladder about the x-axis. The four ladders used in the June 2003 test beam occupied the four central positions; in October 2003, the downstream ladder (position 6) occupied the adjustable position.

The position resolutions corresponding to the narrow Gaussian residual widths (s_1) are $10{:}7 \pm 0{:}3$ and $28{:}6 \pm 0{:}8$ mm for the p- and n-sides. The small difference (~1 mm) observed in the p-side resolution for the two test beams is consistent with the difference observed between the 3 and 4 ms p-side results in June 2003 (Fig. 14). The resolutions corresponding to the area-weighted average residual widths (s) are $16{:}2 \pm 0{:}7$ and $31{:}7 \pm 1{:}0$ mm, respectively.

The proton cluster characteristics of the October 2003 data are listed in Table 4. A comparison with the results reported for June

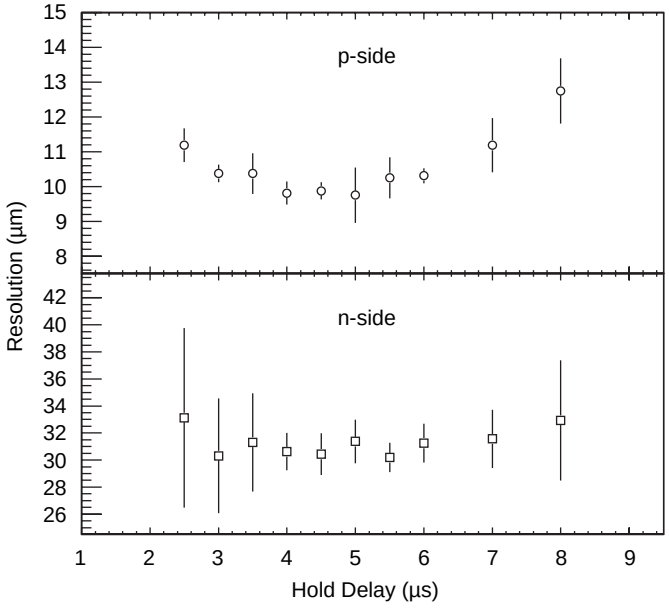

Fig. 14. Position resolution as a function of the VA hold delay.

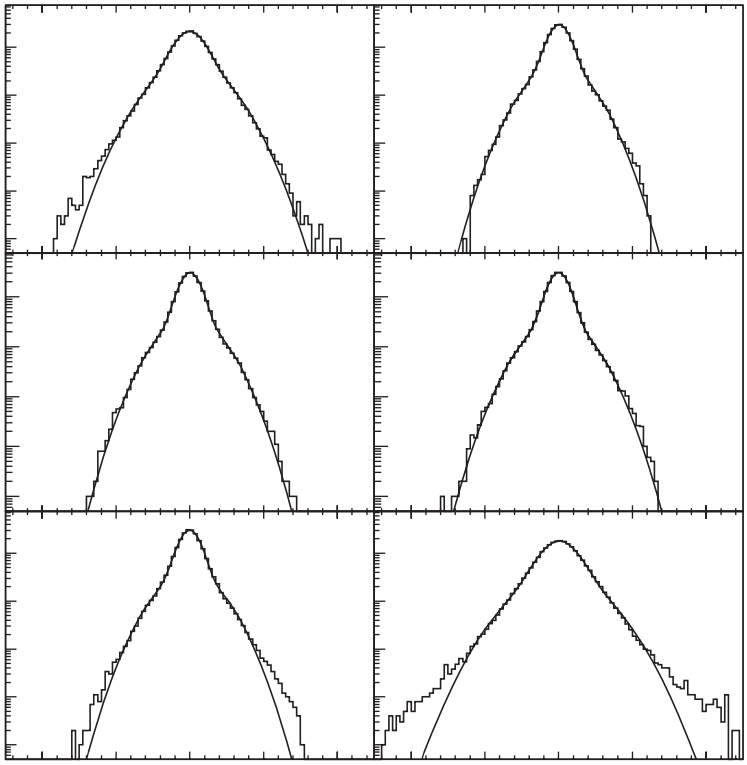

Fig. 15. The p-side residual distributions (five point fit) at the six ladder positions for the proton data of the October 2003 test beam. The residual distributions are described with a sum of two Gaussians; the narrower Gaussian width (s_1) and the area-weighted average width of the two Gaussians are indicated (s_{12}).

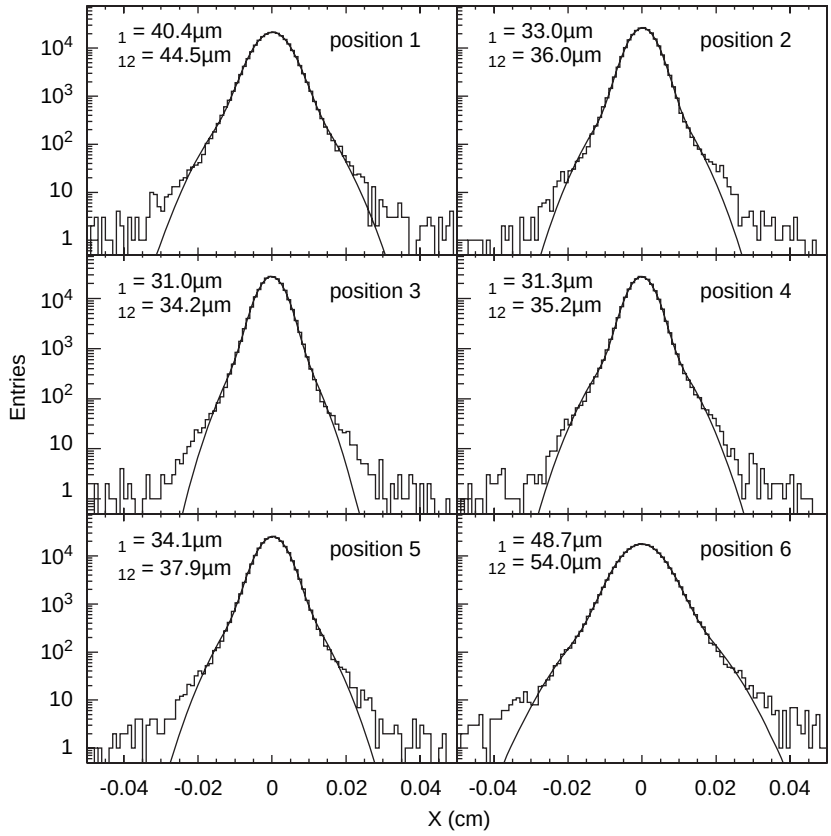

Fig. 16. The n-side residual distributions (five point fit) at the six ladder positions for the proton data of the October 2003 test beam. The residual distributions are described with a sum of two Gaussians; the narrower Gaussian width (s_1) and the area-weighted average width of the two Gaussians are indicated (s_{12}).

2003 indicates the relative influence of the hold delay and temperature on the performance. On the p-side, a 10% lower average channel noise in the October 2003 test beam was accompanied by a 20% lower signal level due to the shorter hold delay, resulting in an overall lower cluster signal-to-noise. On the n-side, the principal difference is the 15% lower noise level due to the lower temperatures of the October 2003 test beam and consequently, an increase in the average cluster signal-to-noise with respect to June 2003.

5.2. Track position and resolution

The quoted position resolutions were obtained with the silicon sensors of the ladders oriented orthogonally to the beam direction. In this configuration, the charge dispersion in the volume of the silicon sensors along the particle pathlength is minimal. The charge collected on the readout strips is affected predominantly by the effects produced at the surface of the silicon by the chosen strip implantation scheme.

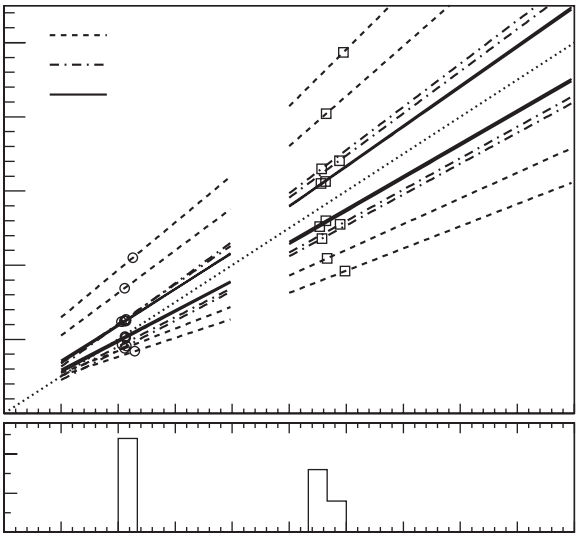

Fig. 17. The relation between proton residual widths and position resolution at the six ladder positions in the October 2003 test beam. The lines with slopes larger (smaller) than unity correspond to the five (six) point track fits. The individual ladder resolutions, corresponding to the experimental narrow Gaussian residual widths, are given by the abscissa values of the data points for the p- (○) and n-sides (&). The distributions of the latter, the average values and standard deviations are shown at the bottom.

The charge created by the normal incidence relativistic protons is collected on two to three strips; the exact number varies with the selection criteria. For example, with a $3s_{ped}$ seed strip threshold and the selection of the highest signal cluster in the case of multiple clusters, the average cluster sizes obtained for the October 2003 data are $2{:}24 \pm 0{:}05$ and $2{:}05 \pm 0{:}03$ strips for the p- and n-sides. The numbers are ~15% lower than the average cluster sizes in Table 4, which were obtained with a $4s_{ped}$ seed threshold and the requirement of a unique np pair in each ladder. No difference is observed in the position resolutions obtained with the two selection criteria.

The proton residual distributions obtained with a five point fit and the $3s_{ped}$ seed strip threshold are shown in Fig. 18 as a function of the impact position (IP). The IP represents the position extrapolated from the fit expressed in terms of the relative position of the particle in the gap between two consecutive readout strips.

The widths of the p-side residual distributions remain relatively constant over the readout gap, with small enhancements in the reconstructed track position appearing at intermediate IP values. At the position of the readout strips, IP equal to zero and one, the residual distributions widen and two distinct enhancements appear along the *y*-axis. Two larger residual tails extend with a similar slope from the gap edges toward the center. The n-side residual distributions display a more significant variation with the track position and a more prominent enhancement at the position of the floating strip at the mid-gap.

A relatively small fraction of the charge is collected on the adjacent readout strips for normal incidence tracks passing near a readout strip. The signal of the neighboring strip approaches the level of the noise, and an eventual incorrect assignment of the second strip will place the track position on the wrong side of the primary strip. The probability of a incorrect assignment decreases toward the center of the gap, whereas the size of the error increases, which explains the observed intensity variation and slope of the larger residual tails.

The non-uniformity observed in the reconstructed beam distribution across the readout gap is explained by the influence of the implantation strip scheme on the charge collection.

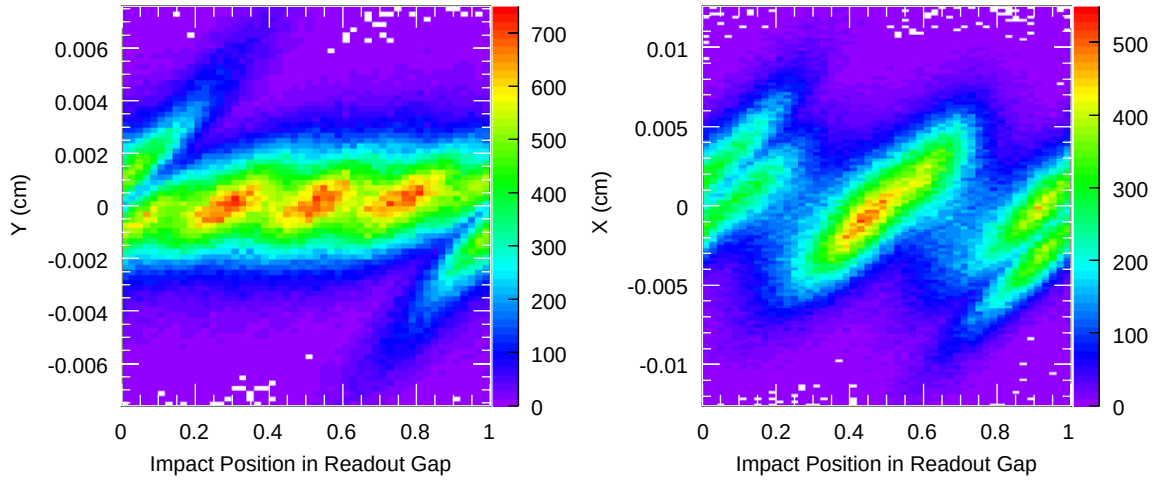

Fig. 18. The p-side (left) and n-side (right) residual distributions at the ladder in position 4 in the October 2003 test beam as a function of the projected track position in the readout gap (impact position).

The presence of the floating strips between the readout strips introduces a capacitive coupling which improves the charge collection across the gap and affects the relation between the particle position and the relative charge seen on the readout strips. The latter can be expressed in terms of Z,

$$Z = \frac{S_2}{S_1 + S_2}$$

where S_1 and S_2 represent the signals of the two highest signal-to-noise strips of the cluster identified by their readout order.

The two strip signal-weighted, or center-of-gravity (COG) position X_{COG} is given by

$$X_{COG} = X_1 + pZ$$

where X_1 is the first strip position and p the readout strip pitch. The above formulation supposes a linear correlation between the relative charge collected on the two strips and the track position in the readout gap, i.e. a uniform, or flat, Z distribution.

The normalized Z distributions, $f(Z)$, for protons and helium nuclei are shown on the left in Fig. 19. Relative enhancements in the distributions are observed at the Z values corresponding to the positions of the floating strips. For a uniform beam distribution at the level of the inter-readout-strip distance, or more generally in the case of a symmetric beam, the Z distribution is obtained by summing the individual inter-strip distributions. The observed behavior indicates a non-linear response, which may be taken into account by integrating the function $f(Z)$ to extract the track position X_Z [13],

$$X_Z = X_1 + p \int_0^Z f(Z')\,dZ'.$$

The integral values of $f(Z)$ across the readout gap are shown on the right in Fig. 19.

The effect of the non-linear charge collection on the reconstructed track position is illustrated in Fig. 20. In general, the difference between a linear interpolation and the position obtained by an integration of the Z function represents a relatively small correction of the reconstructed position for singly charged, minimum ionizing particles [14]. In terms of the position

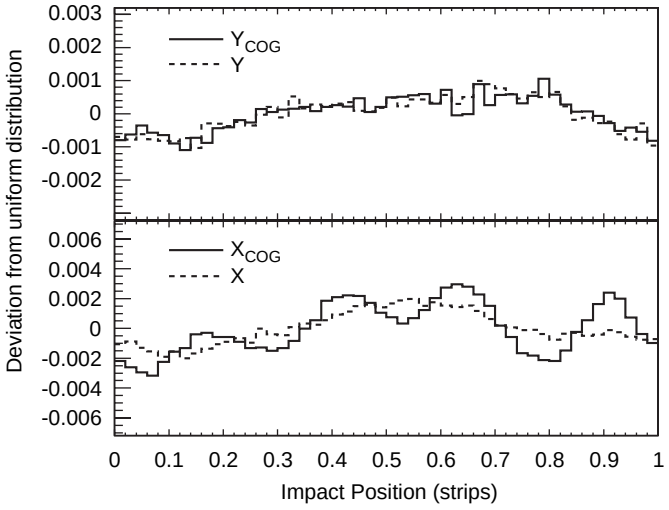

Fig. 20. The reconstructed impact position on the p- (top) and n-sides (bottom) of the ladder at position 2 obtained with the center-of-gravity (COG) and $f(Z)$ (dashed line). The bin contents represent the fractional difference with respect to a uniform distribution.

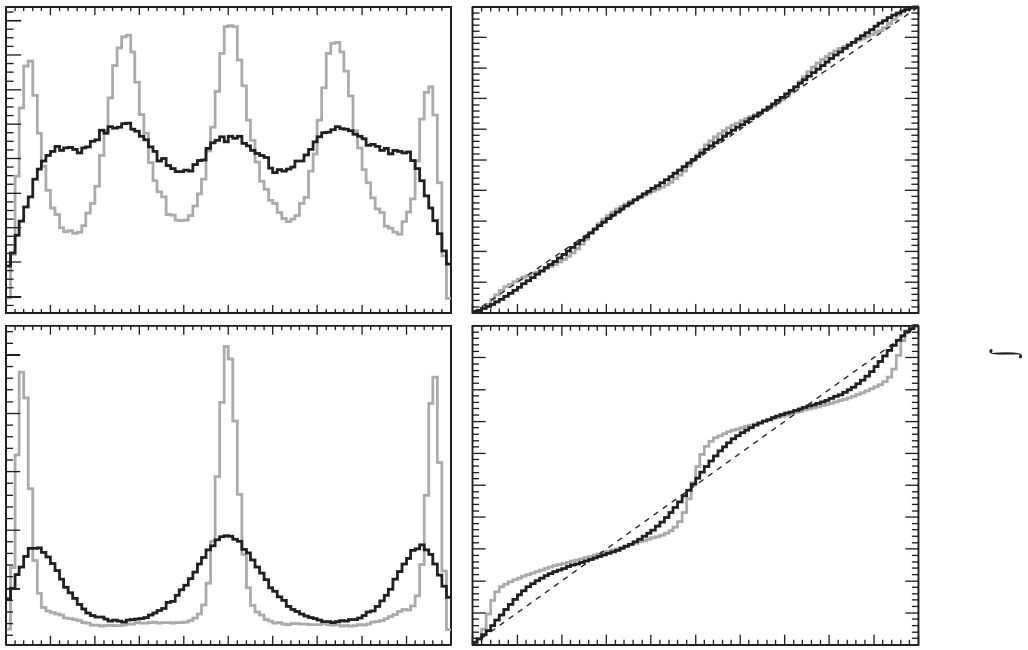

Fig. 19. On the left, the proton and helium normalized Z distributions of the p- (top) and n-sides (bottom); on the right, the integral values of $f(Z)$ which describe the correlation between the track position in the readout gap and relative signal amplitudes of the two strips. The dashed lines of unit slope indicate the appropriate correlation for the position obtained with the center-of-gravity of the strip signals.

resolution, a marginal improvement is observed on the p-side of the AMS-02 ladders for the narrow Gaussian residual widths ($-0{:}1\,\mu m$) and the area-weighted average widths ($-0{:}2\,\mu m$). On the n-side, a small improvement is seen for the narrow Gaussian widths ($-1{:}0\,\mu m$), while the area-weighted average widths increase ($+2{:}5\,\mu m$).

Fig. 21 shows the track residual distributions in the different regions of the readout gap. The position dependent resolution is responsible for the multiple-Gaussian shape of the residual distributions presented in the preceding section. Consequently, the detector performance is expressed in terms of an optimal resolution corresponding to the narrow Gaussian residual width and an effective resolution associated with the area-weighted average of the two Gaussian widths. The narrow Gaussians represent ~75% and ~90% of the residual distributions on the p- and n-sides, respectively.

6. Detection efficiency

The detection efficiency with respect to the cluster seed strip threshold was evaluated for singly charged relativistic particles with the October 2003 proton beam data. The efficiency and multiplicity of noise-induced hits is determined by counting the number of clusters found inside (N^{in}) and outside (N^{out}) a fiducial window of $\pm 300\,\mu m$ around the predicted IP, which is obtained with a five point fit excluding the ladder under consideration. For a given seed threshold and N_{ev} single track events, the efficiency of each ladder is defined as $= N^{in}/N_{ev}$.

The average detection efficiency and the average mean number of noise clusters per event (N_i^{out}/N_{ev}), as a function of the seed strip threshold, are shown in Fig. 22. The error bars correspond to the standard deviations of the results obtained with the six ladders.

An average ladder detection efficiency for the AMS-02 tracker can be defined in terms of the acceptable level of noise clusters. A $3s_{ped}$ seed strip threshold applied to the p-side yields on average one noise cluster per ladder in the 192 ladder tracker, while a $4s_{ped}$ threshold limits the number of p-side clusters to ~5 per event, with a corresponding detection efficiency exceeding 95%. On the n-side, the same average noise level and detection efficiency is obtained with a lower threshold ($3{:}8s_{ped}$). The tracker readout electronics allows to set the threshold limits for each side of each ladder.

7. Specific energy loss

The silicon tracker provides multiple measurements of the specific energy loss which are combined with the velocity measurements of the TOF system and the RICH detector to determine the particle charge. The data of the October 2003 test beam have been used to evaluate the performance of the silicon

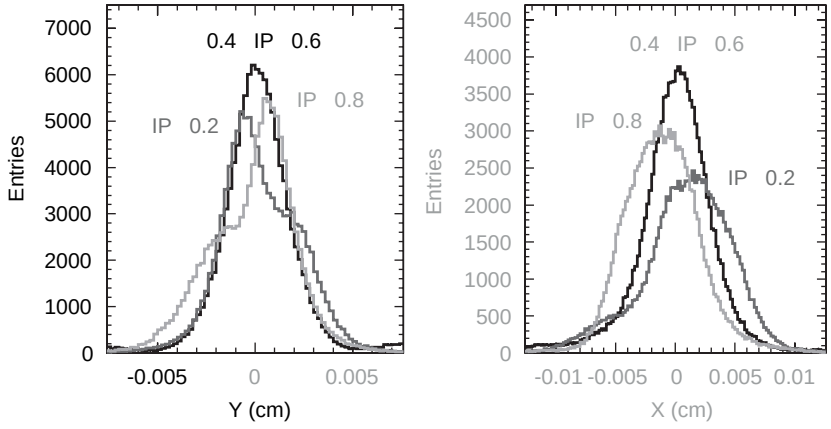

Fig. 21. The p-side (left) and n-side (right) residual distributions (Fig. 18) for three selected regions in the readout gap.

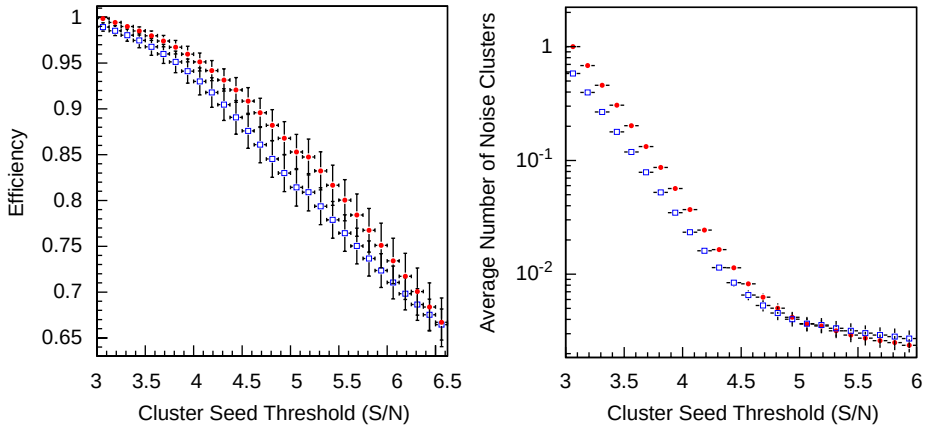

Fig. 22. On the left, detection efficiencies of the p- (•) and n-sides (&) as a function of the cluster seed threshold. On the right, the average number of noise clusters for the p- (•) and n-sides (&) as a function of the cluster seed threshold.

for charge identification of singly and doubly charged relativistic particles.

7.1. Track position and charge collection

The behavior of the average total proton cluster charge across the readout gap is shown in Fig. 23. The collected charge depends on the position of the particle with respect to the readout strips, with the maximal and minimal signals observed at the edges and center of the gap. The values appearing in the figure on the left side represent the average of the mean values of the distributions of the six ladders; the error bars correspond to the standard deviations.

The position sensitivity of the collected charge is more pronounced on the n-side with a relative decrease of ~25% observed in the center of the gap compared to ~15% on the p-side. The difference is explained by the different readout pitches and the presence of the p^+ blocking strips on the n-side which minimize the influence of the surface charge accumulated between the external oxide layer and the silicon; the charge carriers (electrons) are the same type as those responsible for the parasitic charge at the silicon–oxide interface. The above situation is modified in the presence of inclined tracks [10]; the influence of the strip implantation scheme is maximal at normal incidence.

A Landau distribution convoluted with a Gaussian noise contribution has been used to describe the specific energy loss distributions for the determination of the most probable energy loss (Fig. 8). The region of highest energy loss is better described by an exponential tail which is added to the Gaussian-convoluted Landau to describe the cluster charge distributions. Separate fits are used to describe the distributions in the central and edge regions of the readout gap as illustrated in Fig. 23.

7.2. Charge selection

The ion beams at the CERN SPS were composed of secondary nuclei produced by the interactions of Pb nuclei on a Be target which were selected as a function of their atomic-number-to-charge ratio (A=Z). The energy lost in the silicon can be used to distinguish the charge of the relativistic nuclei from $Z = 1$ to 26 [15]. In the present work, the capability to identify the lowest charge particles is evaluated, and used subsequently to select and study the performance for helium nuclei.

The deuterons, helium and lithium nuclei in the secondary ion beams are identified using a maximum likelihood method to determine the compatibility of the measured energy losses with those expected for each nuclear charge. The observed energy losses are corrected to take into account the signal amplitude variations at the hybrid level (electronic gain), as well as the variation in the charge collection across the readout gap in the silicon.

The corrections are determined with selected samples of the different nuclei obtained with the following criteria: a seed (neighbor) strip threshold of $3s_{ped}$ (s_{ped}), a total collected charge for each cluster corresponding to relativistic light nuclei (o 1000 ADC counts), a pn cluster pair in each ladder, a good w^2 probability for the reconstructed tracks in the two projections and a p-side signal in the ladder at position 6 within a restricted range about the most probable values for the nuclear charges (Fig. 24). The highest signal cluster is selected in case of multiple clusters on the same side of the ladder. An example of the energy loss distribution of the selected helium nuclei is shown in Fig. 25. The proton beam data were used to determine the corrections applied for the deuterons in the secondary ion beams.

The values of the most probable energy loss, obtained with a fit consisting of a Gaussian-convoluted Landau distribution and exponential tail, are used to determine the correction factors applied to the measured energy loss. The position dependence of the charge collection for the selected helium nuclei is shown in Fig. 26. The average variations in the collected charge between the central and edge regions of the p- and n-sides of the readout gap are 10% and 35%. The average variations in the electronic gains of the hybrids are 4% and 2.5%, respectively, for the singly and doubly charged particles.

The normalized energy loss distributions of the ladder in position 1 are used to define the probability density function P_Z. The likelihood for a given particle charge Z is given by

$$L_Z = 1 + \sum_{i=1}^{N} \frac{\log(P_Z(x_i))}{\log(10^{-50})}$$

where the x_i are the corrected specific energy loss measurements of the ladders. The lower limit is defined to avoid computational underflows. With this definition L_Z is confined to the range [0; 1], larger values corresponding to higher likelihood.

In order to evaluate the separation power of the likelihood method, it is necessary to have pure samples of protons, helium

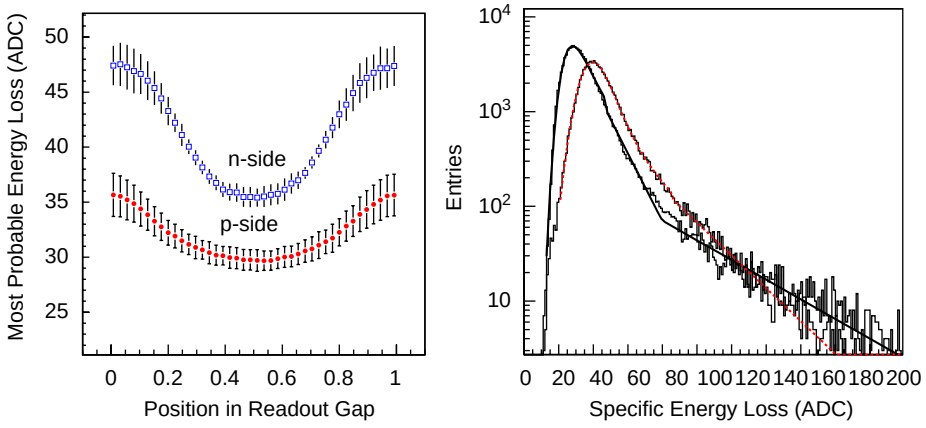

Fig. 23. On the left, the most probable specific energy loss as a function of the proton position in the readout gap for the p- (•) and n-sides (&). On the right, the proton specific energy loss on the n-side of the ladder in position 3 in the October 2003 test beam, and the Gaussian-convoluted Landau fit (including a high energy exponential tail) which is used to describe the energy loss distribution in the two regions of the readout gap: IPo 0:2 and IP4 0:8 (dashed line) and 0:4p IPp 0:6 (solid line).

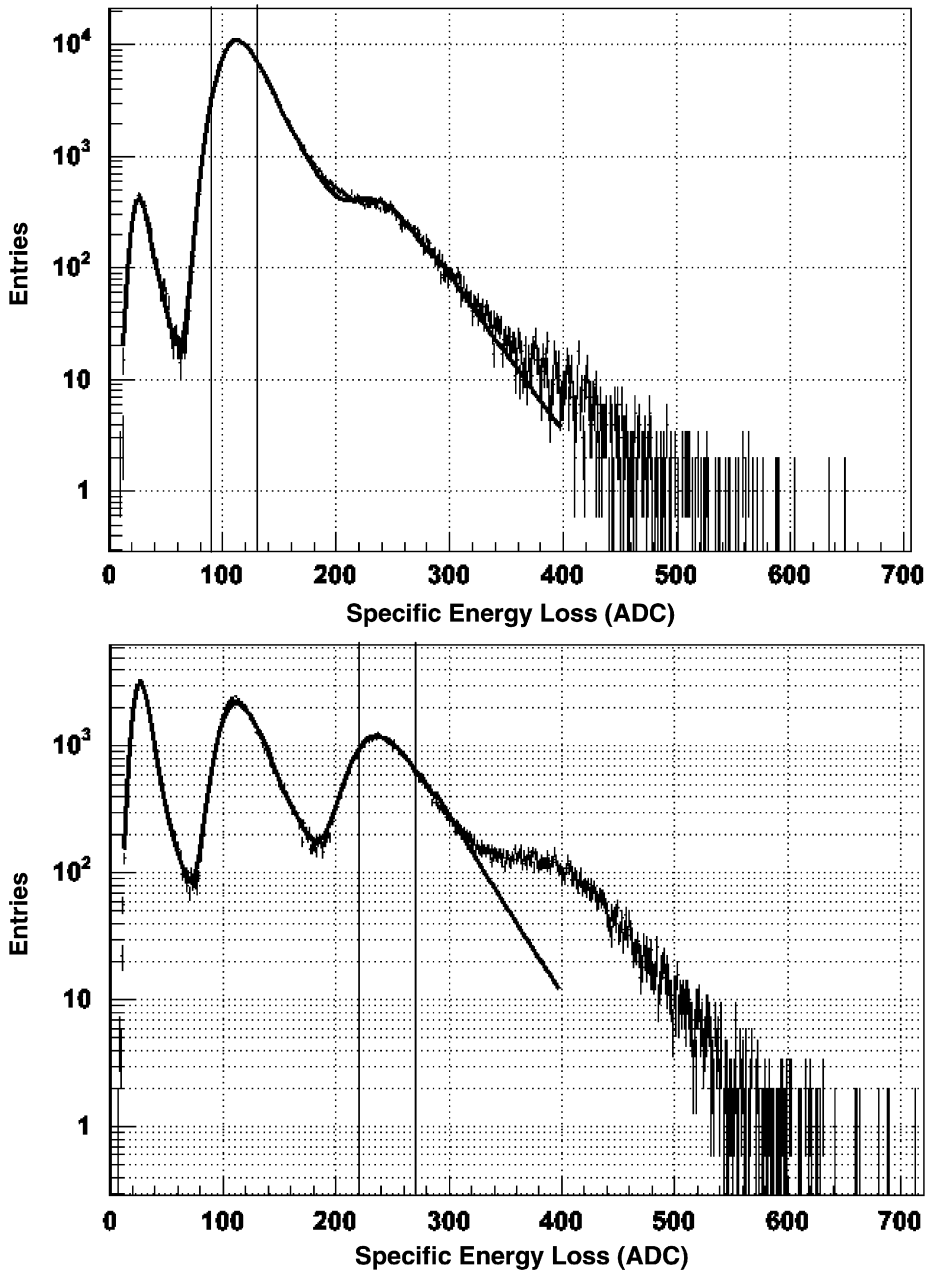

Fig. 24. The p-side specific energy loss distributions of the ladder in position 6 in the A=$Z = 2$ (top) and A=$Z = 2$:25 (bottom) secondary ion beams; the vertical lines denote the regions defined to select the helium (^{4}He) and lithium (^{7}Li) samples. The relative absence of lithium in the A=$Z = 2$ beam is due to the short half-life (0.84 s) of ^{8}Li. A combined fit of the data including the deuteron, helium and lithium energy loss distributions yields the relative normalization constants for each nuclei.

and lithium nuclei. The former are provided by the proton beam data, whereas "pure" helium and lithium samples are identified in the A=$Z = 2$ and 2.25 ion beams using the same selection criteria applied for the determination of the signal level corrections.

The purity of the selected helium and lithium samples is estimated by fitting the combined specific energy loss distribution with the sum of the probability density functions (P_Z) of the deuteron, helium and lithium nuclei (Fig. 24). The probability density function of the proton beam data is used for the deuteron. The estimated purities are given in Table 5.

The maximum likelihood ratio

$$L^{p=n}_{Z;Z+1} = \frac{1 - L^{p=n}_Z}{(1 - L^{p=n}_Z) + (1 - L^{p=n}_{Z+1})}$$

is used to distinguish charge Z and $Z + 1$. Separate likelihood ratios are calculated using the specific energy loss measured on the p- and n-sides of the first five ladders.

The distributions of the two likelihood ratios for the selected proton and helium nuclei samples are shown in Fig. 27. The selection criteria result in identification efficiencies of 99.8% for the singly and doubly charged particles. No proton is identified as helium, while the number of misidentified helium nuclei (60) is compatible with the estimated deuteron contamination in the helium sample (54).

The likelihood distributions for the helium and lithium samples are shown in Fig. 28. The identification efficiencies are 98.7% and 99.5%, respectively, for the two nuclei. The number of helium nuclei identified as lithium (8) corresponds to a contamination level of 10^{-5}, whereas the estimated lithium background in the helium sample is two orders of magnitude smaller. With the

estimated helium background in the lithium sample (771), the number of lithium nuclei identified as helium (885) represents a contamination level of 0.2%.

8. Performance for helium nuclei

The position resolution for helium nuclei has been studied in the secondary ion beams at the CERN SPS (October 2003 data) with the helium sample obtained with the selection criteria described in the previous section. The helium nuclei residual distributions (five point fit) obtained at the ladder in position 2 are shown in Fig. 29. The track positions are given by the signal-weighted mean (COG) of the two highest adjacent signal-to-noise strips. The p-side residual distributions are described by a sum of three Gaussians.

8.1. Position resolution

The average resolutions of the six ladders corresponding to the narrowest Gaussian width, the area-weighted average of the two narrower Gaussian widths and the area-weighted average of the three Gaussian widths are $3{:}9 \pm 0{:}2$, $5{:}3 \pm 0{:}2$ and $6{:}5 \pm 0{:}2$ mm, respectively. The area of the narrowest Gaussian and the summed area of the two narrower Gaussians represent 64% and 96% of the total area of the three-Gaussian fits.

A multiple Gaussian fit of the n-side residual distributions results in a non-negligible spread of the peak positions about zero, consequently the Gaussian widths do not represent

Table 5
The estimated purities of the helium and lithium samples selected in the $A=Z=2$ and 2.25 data

Sample	D (%)	He (%)	Li
He ($A=Z=2$)	0.02	99.98	o 10^{-7}
Li ($A=Z=2{:}25$)	0.01	1.78	98.21

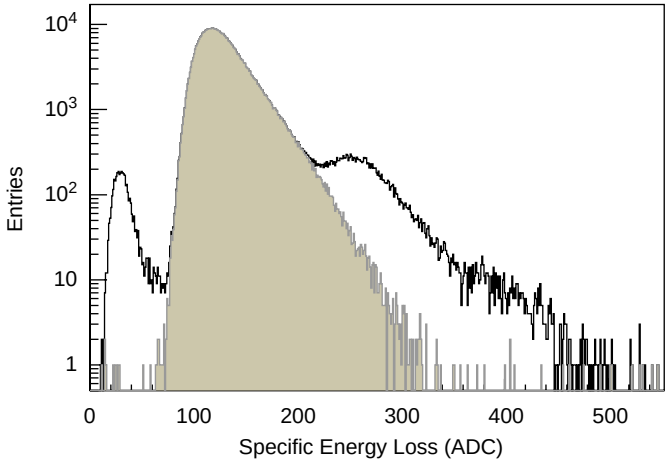

Fig. 25. The p-side specific energy loss distribution of the ladder in position 2 in the $A=Z=2$ nuclei beam obtained with the light ion selection criteria (unshaded) and the distribution of the selected helium nuclei (shaded).

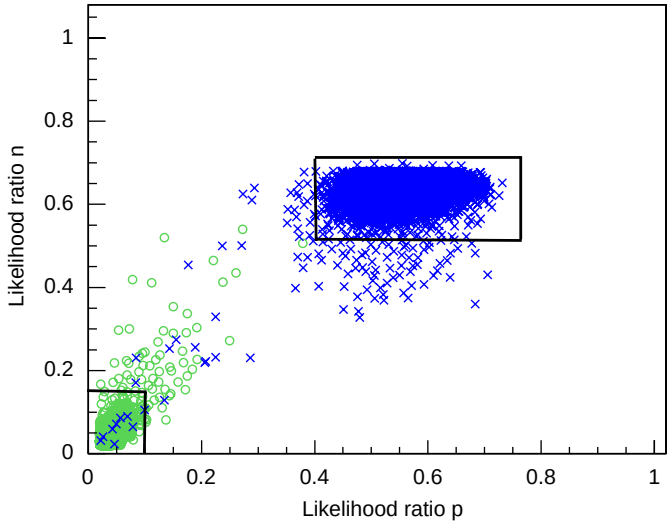

Fig. 27. The distribution of the likelihood ratios, $L^{n}_{1;2}$ and $L^{p}_{1;2}$, computed for the proton (○) and helium nuclei (×) samples. The boxes denote the charge selections applied to determine efficiencies and contamination levels for the singly and doubly charged particles.

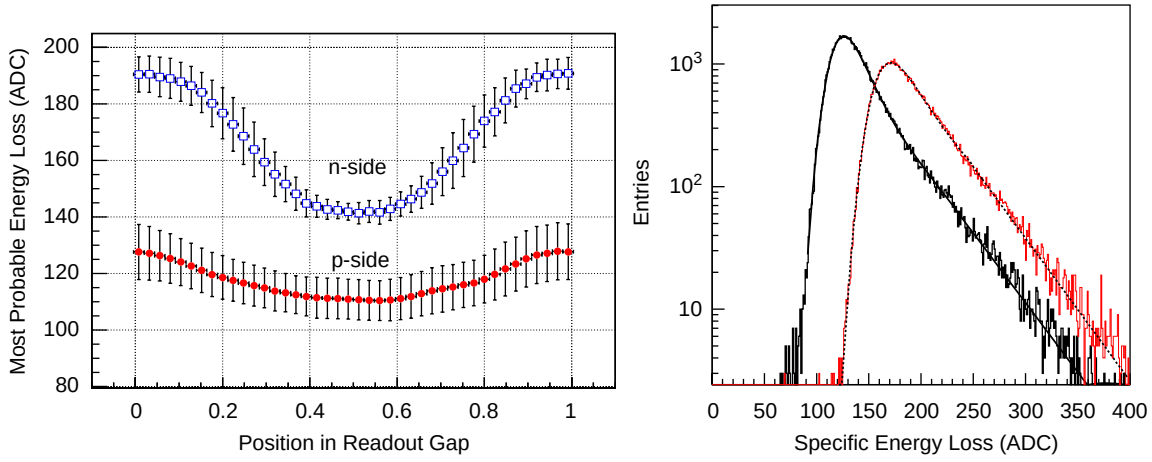

Fig. 26. On the left, the most probable energy loss as a function of the position of the helium nuclei in the readout gap for the p- (•) and n-sides (&). On the right, the measured helium specific energy loss on the n-side of the ladder in position 3 in the October 2003 test beam, and the Gaussian-convoluted Landau fit (including an exponential tail) which is used to describe the energy loss distribution in the two regions of the readout gap: IPp 0:2 (dashed line) and 0:4p IPp 0:6 (solid line).

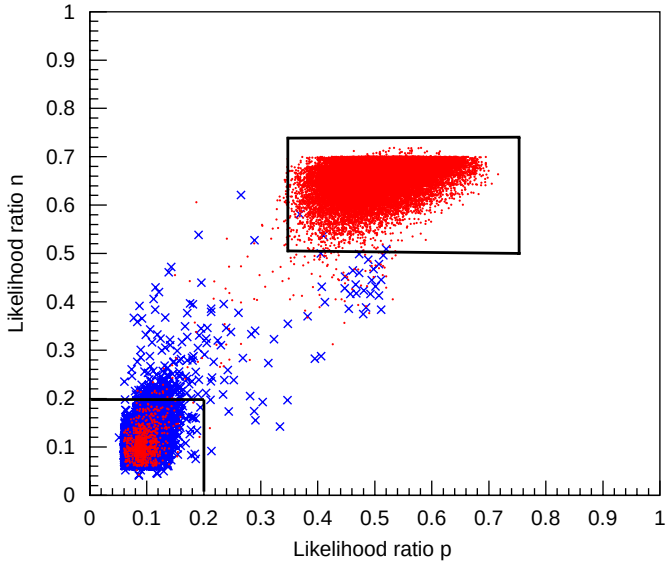

Fig. 28. The distribution of the likelihood ratios, $L^{n}_{2;3}$ and $L^{p}_{2;3}$, computed for the helium (×) and lithium (·) nuclei samples. The boxes denote the charge selections applied to determine efficiencies and contamination levels for the two nuclei.

completely the dispersion observed in the data. A more accurate estimate of the resolution is obtained by comparing the standard deviations of the residual distributions with the simulation results, yielding an average effective n-side resolution of $25{:}3 \pm 2{:}0\,\mu m$.

8.2. Track position and resolution

The behavior of the helium nuclei residual distributions across the readout gap is shown in Fig. 30. As indicated by the Z distributions in Fig. 19, the non-linearity of the charge collection increases with particle charge resulting in an enhancement of the features characterizing the position dependent resolution. In particular, a non-linear response is evident on both sides of the silicon (Fig. 31).

As illustrated in Fig. 32, the multiple Gaussian description may be applied to the n-side residual distributions when the non-linear response is taken into account for the determination of the track position. The resulting average n-side resolutions are $14{:}5 \pm 2{:}3\,\mu m$ (s_1^{res}) and $25{:}5 \pm 2{:}6\,\mu m$ (s_{123}^{res}). The narrowest Gaussian area represents 33% of the total. The effect of the correction of the non-linear response on the previously quoted p-side resolutions is marginal: $-0{:}3\,\mu m$ for s_1^{res} and $-0{:}1\,\mu m$ for s_{123}^{res}.

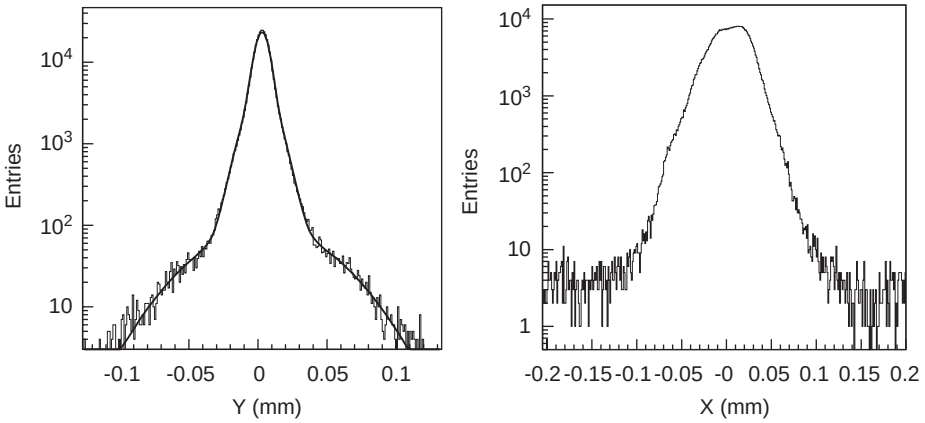

Fig. 29. The p-side (left) and n-side (right) helium residual distributions at the ladder position 2; the former is described by a sum of three Gaussians.

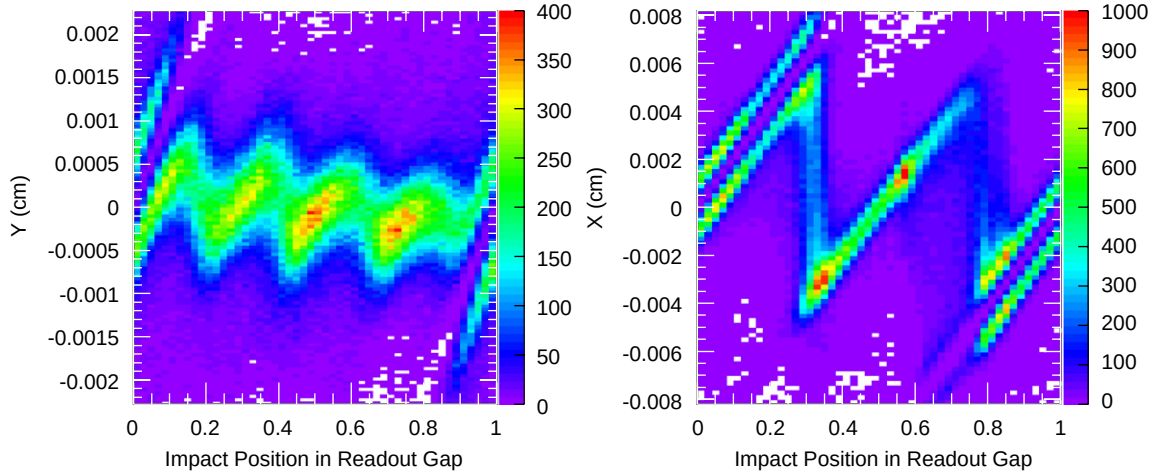

Fig. 30. The p-side (left) and n-side (right) helium nuclei residual distributions at ladder position 2 in the October 2003 test beam as a function of the projected track position in the readout gap (impact position).

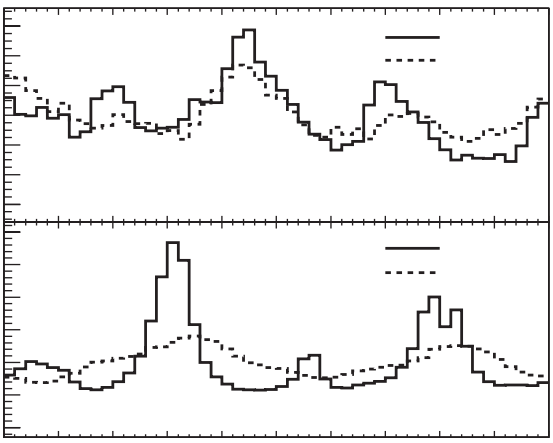

Fig. 31. The reconstructed impact position of the helium nuclei tracks on the p- (top) and n-sides (bottom) of the ladder at position 5 obtained with the center-of-gravity (COG) and $f(Z)$ (dashed line). The bin contents represent the fractional difference with respect to a uniform distribution.

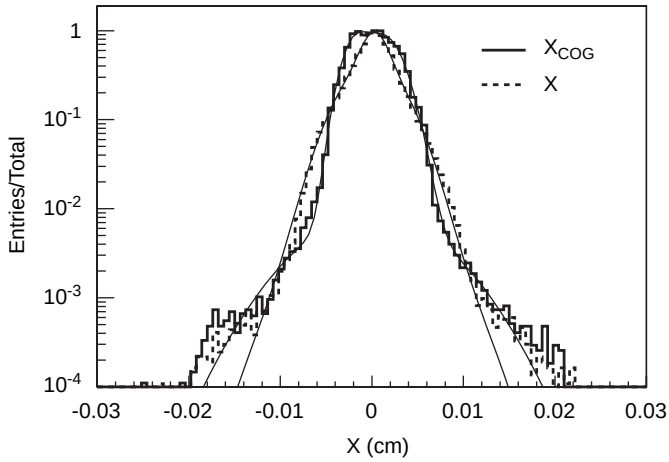

Fig. 32. The n-side helium nuclei residual distributions, and corresponding three-Gaussian fits, at the ladder in position 5 obtained with the two-strip center-of-gravity (COG) and $f(Z)$.

The helium nuclei cluster strip multiplicities are $4{:}9 \pm 1{:}3$ and $4{:}4 \pm 1{:}0$, respectively, for the p- and n-sides. On both sides of the silicon, the best resolution performance (normal incidence tracks) is obtained with a position determination based on the information of the two highest signal-to-noise strips.

9. Operation on the ISS

The particle beam results are used to evaluate the tracker performance on the ISS relative to the thermal environment, the large angular acceptance of the silicon tracker and the restrictions imposed by the limited data bandwidth.

9.1. Thermal environment

On the ISS, the AMS thermal environment is conditioned by the energy radiated by the Sun, including an albedo component from the Earth and the heat dissipated by the detector electronics. In particular, the tracker frontend hybrids located close to the magnet represent an important concern for the detector performance. The heat generated by the ladder hybrids is evacuated by conduction to the exterior of the magnetic field volume by the aluminum cooling bars shown in Fig. 4. Copper braid is used to link the cooling bars of neighboring planes.

9.1.1. Past experience: AMS-01

The temperatures recorded on the inner wall of the AMS-01 permanent magnet varied between 8 and 23 1C during the 10-day shuttle flight. The variation was caused by changes in the relative orientation of the detector with respect to the Sun and the Earth, including a period of several days in the shadow of the Mir space station [16]. The passages between sunlight and shadow over the 90 min orbital period had a negligible influence on the temperatures recorded at the detector.

The AMS-01 tracker consisted of six single layer planes equipped with 57 ladders. The planes were arranged symmetrically about the center of the magnet with planes 1 and 6 located outside the magnet cavity.[8] The temperatures of the hybrids of the ladders were systematically higher than the temperature at the inner magnet wall: +9–10 1C at planes 3 and 4, +6–7 1C at planes 2 and 5, +6 °C at plane 6, and +5 °C at plane 1. Temperature probes located in the middle of the planes 1 and 6 indicated that the temperature of the silicon on the external planes was ~3 °C lower than the corresponding hybrid temperatures.

The tracker power was switched off on four occasions after the separation from Mir due to the high temperatures encountered when the detector was orientated near the zenith direction. No effect was observed on the magnet temperature during these periods, which did not exceed for a single duration 2.5 h (5.5 h in total).

9.1.2. The temperature of the AMS-02 tracker on the ISS

Due to the presence of the AMS-02 superconducting magnet, an active cooling system using a two-phase CO_2 flow has been incorporated in the tracker design to maintain the temperature within the magnetic field volume in the range of −15 to +15 °C. The forseen range takes into account the effect of the orbit-to-orbit changes in the relative orientation of the detector with respect to the Sun. The nominal operating temperature of the tracker may be as low as −10 °C.

In order to extrapolate the performance results of the particle beam measurements to the temperature range of the ISS, two AMS-02 ladders have been operated in a thermal chamber (−30 to +40 °C).[9] The calibration results, shown in Fig. 33, are consistent with the temperature variation of the noise observed over the limited range in the June 2003 test beam. The most significant effect on the single channel noise (~15%) is observed on the n-side between 40 and 20 °C, whereas the total leakage current of the ladders decreases by a factor of 20 between 40 and −30 °C.

The two ladders available for the thermal tests were each equipped with a poorer quality hybrid; the designations n (p) in Fig. 33 refer to the ladder with the good quality n (p) hybrid. The former displays a linear temperature dependence with the logarithm of the leakage current in agreement with previously reported results [17]; the latter has a lower leakage current which deviates from the expected behavior below ~10 °C. The single channel noise appears rather insensitive to the leakage current at temperatures below ~25 °C.

The thermal behavior of the single channel noise and the position resolution as a function of the cluster signal-to-noise

[8] The AMS-02 superconducting magnet was designed to reproduce the field geometry of the AMS-01 permanent magnet.

[9] SERMS, 21 via Pentina Bassa, 05100 Terni, Italy.

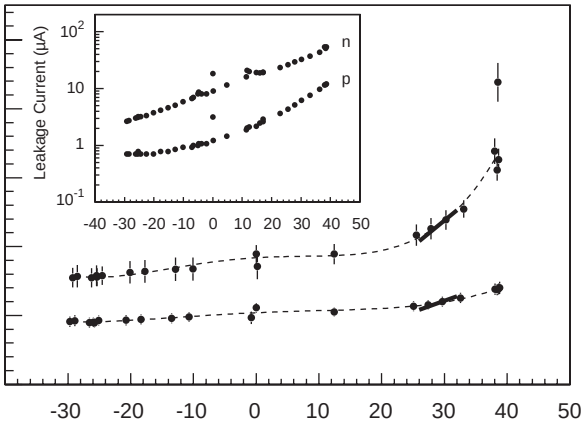

Fig. 33. Temperature dependence of the average channel noise: polynomial fit of the thermal chamber measurements (dashed lines) and the temperature dependence measured in the June 2003 test beam (solid lines). The corresponding leakage currents are shown in the inset figure.

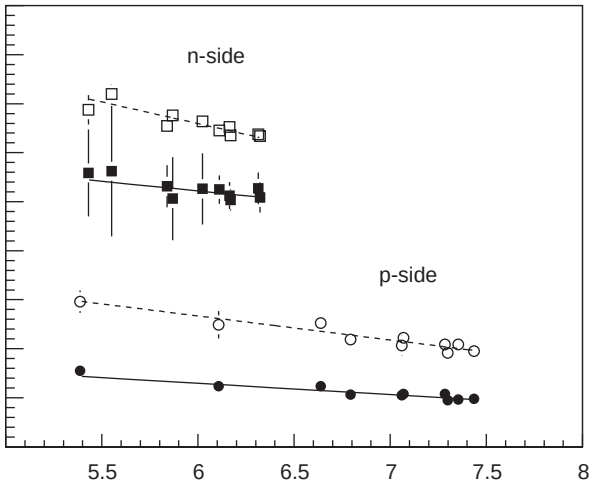

Fig. 34. Optimal (closed symbols) and effective (open symbols) position resolutions as a function of the cluster signal-to-noise from the June 2003 proton data.

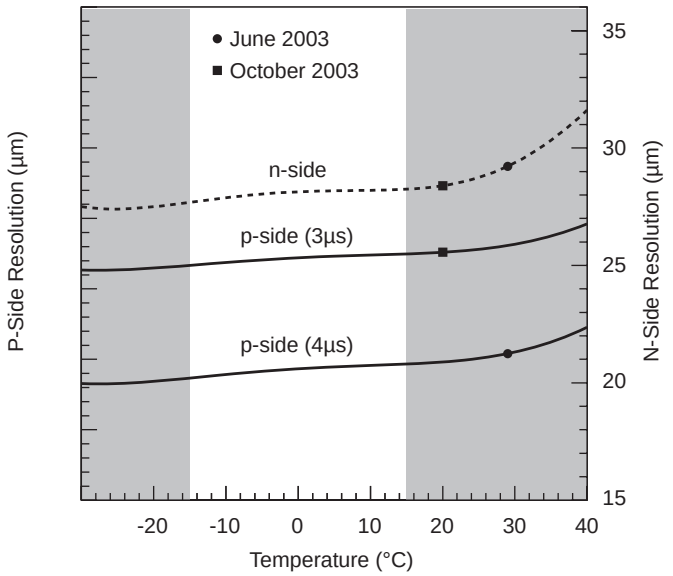

Fig. 35. Position resolution for singly charged relativistic particles (normal incidence) as a function of the temperature; the p-side (solid) and n-side (dashed) resolutions are indicated on the left and right, respectively. Results for delay hold times of 3 and 4 μs are shown for the p-side. The operating conditions and corresponding resolutions are indicated for the June and October 2003 test beams. The unshaded region corresponds to the expected operating temperature range of the tracker on the ISS.

Table 6
The proton p-side position resolutions at the non-inclined ladder positions used in the simulation to estimate the inclined ladder resolution in the October 2002 data

Resolution (μm)	Ladder position				
	2	3	4	5	6
Optimal	13.2	9.7	13.2	11.0	11.5
Effective	22.0	14.4	22.0	17.0	18.5

(Fig. 34) are used to predict the temperature variation of the resolution. The results, shown in Fig. 35, indicate no significant effect on the resolution with respect to the expected operating temperature range on the ISS. Consequently, no significant difference in performance is expected from the particle beam results. In comparison, the 1 μm change produced by a 1 μs difference in the VA hold delay on the p-side appears more significant (Fig. 35).

The TDR crate and power supplies were located outside the thermal chamber. An eventual influence on the performance due to the temperature of the TDR crates located outside the magnet volume cannot be excluded. However, the electronics located outside the magnet is expected to operate at temperatures comparable to normal operating conditions on the ground.

9.2. Inclined tracks

In accelerator-based applications, the acceptance of the silicon microstrip detectors is dominated by near normal incidence tracks due to the presence of an interaction point (vertex) and a corresponding optimization of the detector geometry. Deviations from normal incidence imply a greater dispersion of the collected charge which may affect the spatial resolution [18]. The presence of inclined tracks in the large acceptance cosmic-ray detector may be expected to affect the performance of the AMS-02 silicon tracker.

The influence of the track angle on the position resolution of the singly and doubly charged particles has been studied in the proton and secondary ion beams at the CERN SPS in October 2002. The ladder in the first (upstream) position of the six ladder telescope was rotated by 15° and 30° about the x-axis, thus providing inclined track data to study the effect on the p-side position resolution. The resolution of the inclined ladder is obtained by comparing the two-Gaussian residual widths of the data with the corresponding results from the Geant3 simulation, where the resolution of the first ladder is varied and the resolutions of the non-inclined ladders are defined by their most probable cluster signal-to-noise.

In October 2002, the ladders in positions 2 and 4 were equipped with p-side hybrids with abnormally low gain VAs (~65%), a problem which affected several early production ladders. For protons, the p-side resolutions of the non-inclined ladders used in the simulation (Table 6) are based on their cluster signal-to-noise, and the relation between signal-to-noise and position resolution is derived from the June 2003 data (Fig. 34).

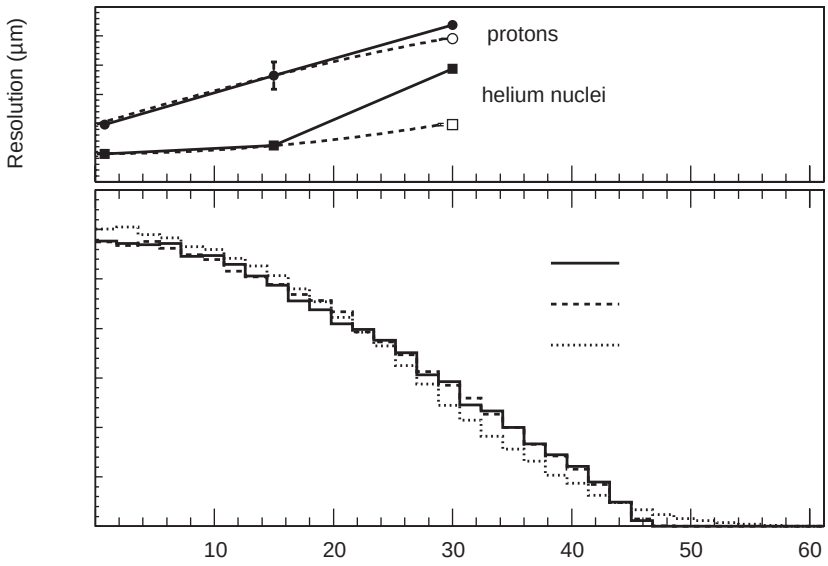

Fig. 36. Position resolutions of the p-side for protons and helium nuclei for different inclination angles with respect to the normal direction of the p-side strips (top), and the inclination angle distributions for three incident rigidities in the geometric acceptance of the AMS-02 tracker. In general, a better resolution is obtained when the position is determined with the two highest signal-to-noise strips of the cluster (closed symbols), with the exception of the largest angle (30°), where three strips are used when present (open symbols).

For helium nuclei, optimal and effective resolutions of 5 and 6:7 mm are used for the non-inclined ladders (multiplied by 1.4 for the low gain ladders in positions 2 and 4).

The angular dependence of the optimal resolutions is shown in Fig. 36. The resolutions reported at 15° and 30° correspond to the average values of the inclined ladder resolution which reproduce in the simulation the residual widths (five and six point fits) of the data in the first three upstream ladders (two for the 15° data). The quoted errors are given by the uncertainties of the residual distribution fit, which are used to delimit the resolution range compatible with the data. The errors are large at the downstream ladder positions where the residual widths are relatively insensitive to the resolution of the most upstream ladder. For the last three ladder positions (four for the 15° data), the simulation predicts a residual width which is compatible with the residual widths of the data.

The same method has been applied to the October 2003 data to determine the p-side resolution at the first (non-inclined) ladder position. The residual distributions of both particles charges are described by the sum of two Gaussians. The results for the optimal resolutions are $10{:}9 \pm 0{:}1$ and $5{:}4 \pm 0{:}1$ mm, respectively, for the singly and doubly charged particles. The values are consistent with the average proton optimal resolution (Fig. 17) and the helium nuclei resolution of the first ladder (5:3 mm). The normal incident angle resolutions quoted in Fig. 36 are the average optimal resolutions for protons, $9{:}8 \pm 0{:}3$ mm from the June 2003 data, and helium nuclei, $4{:}8 \pm 0{:}4$ mm corresponding to the narrow Gaussian of a two-Gaussian fit of the October 2003 data.

The p-side position resolution degrades as the inclination angle increases. The behavior observed with protons is similar to the influence of the track angle on the resolution reported for relativistic electrons, where the quoted resolutions were 4 and 14 mm at 0° and 30° [19]. The factor of two difference between the resolutions of the two measurements is comparable to the difference in readout (implantation) strip pitches of the detectors; the earlier measurement was performed with single-sided silicon sensors with a readout (implantation) strip pitch of 50 (25) mm.

The position resolution is improved at the largest angles when a third strip is included in the COG determination of the track position. The effect is modest for protons, where the average cluster strip multiplicities are 2.6, 2.6 and 3.1 at the three angles. A similar improvement was reported for the angles of 30° and 45° in Ref. [19], when the position algorithm is modified to take into account the full extent of the cluster. In the case of helium nuclei, the average cluster strip multiplicities in order of increasing angle are 4.0, 4.4 and 4.8; the addition of the third strip results in a significant improvement of the resolution at 30°.

Fig. 36 shows the distribution of incident track angles, with respect to the normal direction of the p-side strips, in the geometric acceptance of the AMS-02 tracker. A parametrization of the measured angular resolution folded with the angular acceptance yields average p-side optimal resolutions of 18 and 7 mm for the singly and doubly charged particles.[10]

The estimated AMS-02 rigidity resolutions for proton and helium nuclei are shown in Fig. 37 for tracks with measurements in at least six silicon layers including the two external layers. The performance of the magnetic spectrometer may be characterized by the maximum detectable rigidity (MDR) corresponding to a measurement error of 100%. The MDR values for the singly and doubly charged particles are ~2:2 and ~3:7 TV. In the detector simulation, the *y* position resolution (orthogonal to the principal magnetic field component) is described by two angle dependent Gaussian widths corresponding to the optimal (Fig. 36) and effective p-side resolutions. The latter, as well as the relative weight of the two Gaussians as a function of the angle, are obtained in an analogous manner from the test beam data using the area-weighted average widths. The effective resolutions, averaged over the tracker acceptance, are 21 and 11:5 mm for the singly and doubly charged particles.

[10] A more gradual variation than predicted by the limited number of data points of the present study can be expected between 0° and 15° for singly charged relativistic particles [18].

The tracker alignment may be performed at the ladder level, consequently an alignment uncertainty is added to the position measurement resolution to take into account the relative alignment of the sensors in the ladders. The alignment uncertainty for the p-side strips (4:6 mm), was determined by a high precision metrology (~1 mm) of the AMS-02 ladders [20].

9.3. Bandwidth and data rate

An important limitation for a space-based detector is the bandwidth available for data transmission. The tracker contains 196,608 readout channels generating 2.4 Mbits of information at the output of the ADCs. The forseen bandwidth for the AMS-02 detector is 2 Mbit/s which implies, with an average orbital event rate of 1 kHz, dominated by protons (~90%), a maximum event size of 2.3 kbit. The onboard data processing of the tracker is expected to provide a reduction factor of $\sim 10^3$.

The test beam results for singly charged, minimum ionizing particles (Fig. 22) allow to establish the performance level compatible with the bandwidth restriction. The event size, including noise clusters and track reconstruction efficiency (X 6 silicon layers) as a function of the cluster strip seed threshold are shown in Fig. 38. The previously quoted average ladder thresholds compatible with the noise criteria, 4 and $3{:}8s_{ped}$ for the p- and n-sides (Section 6), satisfy the bandwidth restriction and provide good detection efficiencies. Seed strip thresholds below $3{:}5s_{ped}$ yield unacceptable event sizes, while the detection efficiency degrades above $4{:}5s_{ped}$.

9.3.1. Onboard data processing

The quoted tracker performances are based on an offline analysis of the 2002 and 2003 particle beam data. An extrapolation of the particle beam results to the AMS-02 tracker on the ISS implies an equivalent performance is obtained with the onboard

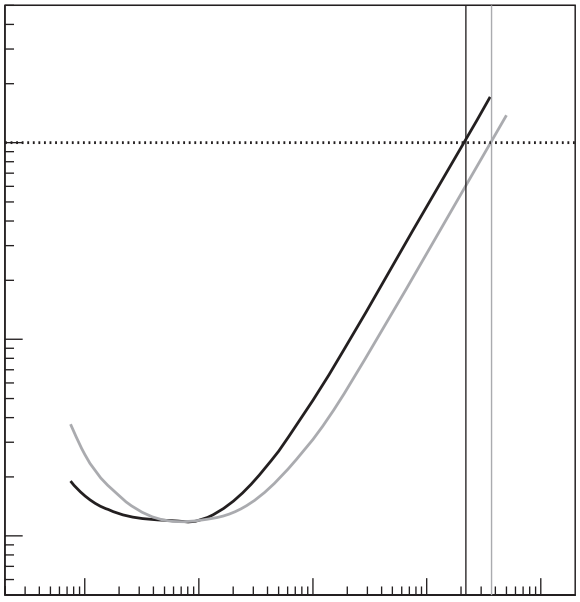

Fig. 37. The expected AMS-02 proton and helium nuclei rigidity resolutions; the values of the maximum detectable rigidity (100% measurement error) are indicated.

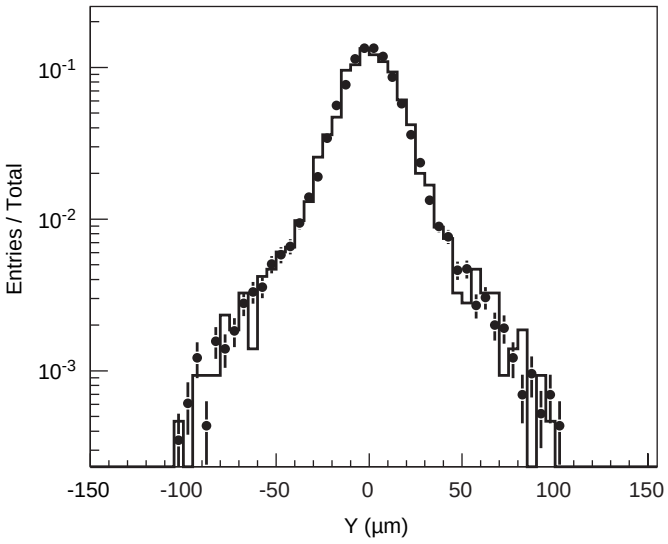

Fig. 39. A p-side residual distribution obtained with online data reduction in a 7 GV electron beam at the CERN PS in September 2004; the histogram corresponds to simulation results obtained with a two-Gaussian description of the position resolution.

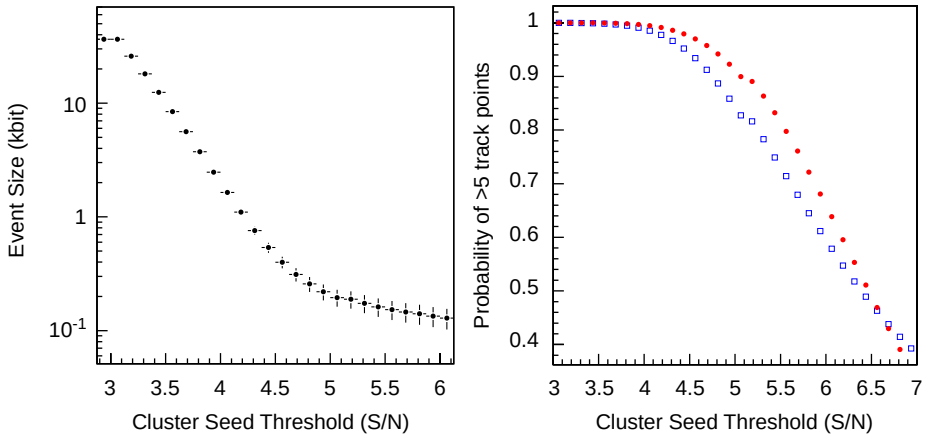

Fig. 38. On the left, the contribution of the tracker noise clusters to the AMS-02 event size as a function of the threshold of the cluster seed strip. On the right, the probability of 4 5 measurements on the p- (•) and n-sides (&) of the ladders along the particle path as a function of the threshold of the cluster seed strip. Threshold levels are expressed in terms of the single channel noise (s_{ped}); the results are based on the ladder performance in the October 2003 test beam (Fig. 22).

data processing, which was tested for the first time in particle beams at the CERN PS in September 2004.

An example of the residual distributions for relativistic electrons is shown in Fig. 39. The observed residual widths correspond to optimal and effective resolutions of $9{:}5 \pm 0{:}2$ and $15{:}3 \pm 0{:}3\,\mu m$ (p-side), and $30{:}7 \pm 0{:}6$ and $34{:}3 \pm 0{:}6\,\mu m$ (n-side). The results were obtained with a preliminary version of the DSP data reduction code and a $5s_{ped}$ seed strip threshold. The corresponding detection efficiencies, $88 \pm 1{:}5\%$ and $80 \pm 2{:}0\%$, are compatible with the performance obtained with an offline analysis of the October 2003 proton data (Fig. 22).

The rather high cluster seed strip threshold was required to compensate the problem encountered with the flight version power supplies, which were used for the first time in the test beam, and the less than optimal TDR calibration. The former was due to a fault in the grounding/isolation between the power supply modules and crate chassis. The TDR calibration data were acquired separately for each ladder, whereas the TDRs are read synchronously during data-taking. The different readout modes imply different power levels which affect the pedestal levels. Given the nature of these problems, no significant difference is expected between the performances of the raw and onboard data processing.

10. Summary

The performance of the AMS silicon tracker for singly and doubly charged particles has been studied in relativistic proton and ion beams. The position resolution, which is dependent on the relative position of the particle with respect to the readout strips, is defined in terms of optimal and effective resolutions, corresponding, respectively, to the narrowest Gaussian width and the area-weighted average width of the multiple Gaussians characterizing the track residual distributions. The results for the two particle charges are summarized in Table 7. The detection efficiency associated with the quoted singly charged minimum ionizing particle resolutions exceeds 95% on both sides of the silicon detector.

The position sensitivity of the resolution is due to the influence of the strip implantation scheme on the charge collection. In the case of the position measurement on the n-side for helium nuclei, the non-linearity in the charge collection must be taken into account in order to apply the multiple Gaussian description.

The measurements of the specific energy loss also display a position sensitivity affecting both the magnitude and the shape of the collected charge distributions. A maximum likelihood method using five measurements of the specific energy loss on both sides of the silicon, corrected as a function of the track position in the readout gap, provided an efficient charge identification of deuterons, helium and lithium nuclei (4 99:8%) in the secondary ion beam, with negligible background contamination.

In the context of a large acceptance cosmic-ray detector, the above performances at normal incidence must be verified for inclined tracks. The angular dependence of the p-side position has been studied. For protons, the resolution degrades by a factor ~2 at the largest measured angle (30°). For helium nuclei, the degradation remains limited (50%) at the 30° angle when a third strip is included in the position determination. The angular dependent position resolutions have been used to evaluate the AMS-02 rigidity resolutions: 1–3% in the rigidity range 1–50 (1–100) GV for protons (helium nuclei) with a maximum detectable rigidity of 2.2 (3.7) TV.

The quoted performances have been obtained with signal thresholds which are compatible with the data bandwidth restrictions of the spaceborne detector. Consequently, and in view of the uniform noise performance observed in the different particle beams with ≈20% of the AMS-02 tracker silicon ladders, the corresponding detection efficiency (4 95%) will result in a ~100% track reconstruction efficiency (X 6 points) for the minimum bias signal (singly charged minimum ionizing particles).

The ground performance results are not expected to be affected by the lower operating temperatures on the ISS. The single channel noise shows little sensitivity to the thermal behavior of the silicon ladders for temperatures below ~25 °C.

Table 7
Position resolutions for normal incidence tracks: effective refers to the resolution corresponding to the area-weighted mean width of the two (proton) and three (helium) Gaussians used to describe the residual distributions, optimal refers to the resolution corresponding to the narrowest Gaussian width representing the quoted fraction of the total area of the multiple Gaussian fit

	Optimal (fraction) (μm=%)	Effective (100%) (μm)
Protons		
p-side	$9{:}8 \pm 0{:}3$ (70)	$15{:}3 \pm 0{:}6$
n-side	$28{:}6 \pm 0{:}8$ (90)	$31{:}7 \pm 1{:}0$
Helium nuclei		
p-side	$3{:}9 \pm 0{:}2$ (65)	$6{:}5 \pm 0{:}2$
n-side	$14{:}5 \pm 2{:}3$ (33)	$25{:}5 \pm 2{:}6$

11. Concluding remarks

Protons and helium nuclei are the dominant cosmic-ray components, representing, respectively, ≈90% and ≈9% of the total particle flux. The performance results for singly charged relativistic particles are relevant for the flux measurements of the relatively rare positrons and antiprotons, as well as for high energy gamma rays which can be detected by pair conversion in the materials preceding the tracker [21].

The specificity of a magnetic spectrometer is the capability to determine the sign of the particle charge. Antihelium searches provide the most stringent limits for the existence of antimatter,

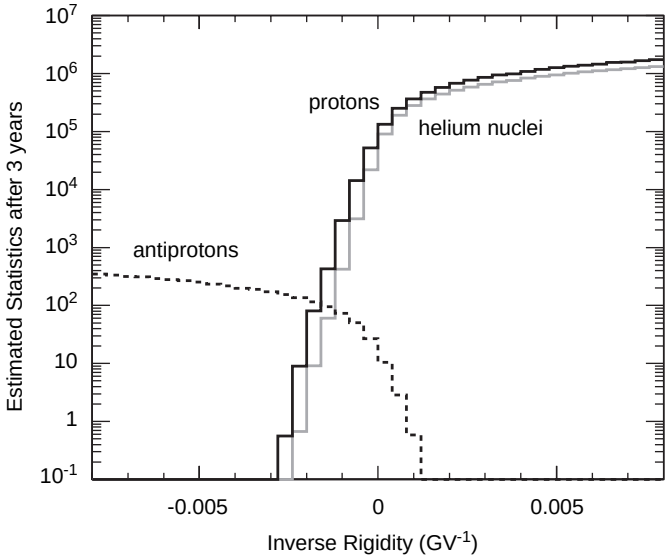

Fig. 40. Antiproton, proton and helium nuclei inverse rigidity distributions expected after three years on the ISS. The antiproton and proton statistics reflect the smaller geometric acceptance of the electromagnetic calorimeter.

whereas precise measurements of the relatively rare singly charged particle spectra may reveal the existence of dark matter.

The reconstructed signed inverse rigidity distributions for protons, antiprotons and helium, corresponding to a three year measurement of the AMS-02 on the ISS, are presented in Fig. 40. The simulated proton and helium fluxes are based on the results of the AMS-01 shuttle flight [1] and the balloon-borne experiments BESS [22] and CAPRICE [23]. The antiproton flux is obtained from an extrapolation to higher energies of the existing data, which is compatible with a constant antiproton-to-proton flux ratio ($\sim 10^{-4}$) above 10 GV [24].

The displayed statistics correspond to the geometric acceptance of the detector, i.e. detection and reconstruction inefficiencies are not taken into account. An electron–hadron rejection factor of o 10^{-4}, provided by the TRD and electromagnetic calorimeter, is required to distinguish antiprotons from electrons. The antiproton and proton statistics in Fig. 40 reflect the limited acceptance of the latter, ~20% of the tracker geometric acceptance. The estimated maximum detectable rigidity for antiprotons, as well as the upper limit for the antihelium search is ~0:5 TV.

Acknowledgements

We wish to thank the technical staffs of the participating institutions and in particular the important contributions of P. Béné, Ph. Bouvier, F. Masciocchi, J.P. Richeux and M. Willenbrock at the l'Université de Genève, and L. Accardo, S. Blasko, S. Bizzaglia, M. Bizzarri, M. Saveri and A. Papi at INFN Perugia, as well as S. Borsini and V. Cascioli at SERMS. This work was funded by the Fonds National Suisse pour la Recherche Scientifique, the Agenzia Spaziale Italiana (ASI), and Deutches Zentrum für Luft und Raumfahrt (DLR).

References

[1] M. Aguilar, et al., Phys. Rep. 366 (2002) 331.
[2] J.B.A. England, et al., Nucl. Instr. and Meth. A 185 (1981) 43.
[3] G. Batignani, et al., Nucl. Instr. and Meth. A 277 (1989) 147.
[4] D. DiBitonto, et al., Nucl. Instr. and Meth. A 338 (1994) 404.
[5] O. Toker, et al., Nucl. Instr. and Meth. A 340 (1994) 572.
[6] N. Dinu, E. Fiandrini, IMTC 2003 Instrumentation and Measurement Technology Conference, vol. 1, Vail, CO, USA, 20–22 May 2003, pp. 786–791.
[7] K. Österberg, Nucl. Instr. and Meth. A 435 (1999) 1.
[8] M. Acciarri, et al., Nucl. Instr. and Meth. A 351 (1994) 300.
[9] G. Barichello, et al., Nucl. Instr. and Meth. A 506 (2003) 217.
[10] J. Alcaraz, et al., Il Nuovo Cimento 112A (11) (1999) 1325.
[11] T. Antičić, et al., Nucl. Instr. and Meth. A 374 (1996) 309.
[12] R. Brun, et al., CERN Report DD/EE/84-1, revised 1987.
[13] E. Belau, et al., Nucl. Instr. and Meth. 214 (1983) 253.
[14] B. Alpat, et al., Nucl. Instr. and Meth. A 439 (2000) 53.
[15] B. Alpat, et al., Nucl. Instr. and Meth. A 540 (2005) 121.
[16] W.J. Burger, et al., Nucl. Instr. and Meth. A 512 (2003) 517.
[17] M.T. Brunetti, et al., Nucl. Instr. and Meth. A 302 (1991) 362.
[18] R. Turchetta, Nucl. Instr. and Meth. A 335 (1993) 44.
[19] Y.-H. Chang, et al., Nucl. Instr. and Meth. A 363 (1995) 538.
[20] W.J. Burger, Nucl. Instr. and Meth. A 582 (2007) 886.
[21] G. Lamanna, Nucl. Phys. B (Proc. Suppl.) 113 (2002) 177.
[22] T. Sanuki, et al., Astrophys. J. 545 (2000) 1135.
[23] M. Boezio, et al., Astropart. Phys. 19 (2003) 583.
[24] I.V. Moskalenko, et al., Astrophys. J. 565 (2002) 80.